

# Chaotic Transport of Mass and Potential Vorticity for an Island Recirculation

PATRICK D. MILLER

*Department of Mathematical Sciences, Stevens Institute of Technology, Hoboken, New Jersey*

LAWRENCE J. PRATT AND KARL R. HELFRICH

*Woods Hole Oceanographic Institution, Woods Hole, Massachusetts*

CHRISTOPHER K. R. T. JONES

*Division of Applied Mathematics, Brown University, Providence, Rhode Island*

(Manuscript received 9 January 2001, in final form 30 May 2001)

## ABSTRACT

The method of lobe analysis is used and extended to analyze a time-dependent, boundary-trapped recirculation. The recirculation gyre occurs in a numerical model of wind-driven flow around an island, but the underlying geometry of the gyre is similar to persistent eddies such as the Alboran Gyre and the Great Whirl. Even in the steady (weak forcing) limit, the gyre leaks fluid due to the fact that the surface Ekman pumping above it is directed downward. The authors show that this leakage is rapidly superseded by chaotic transport into and out of the gyre when time dependence sets in. Variations of the traditional “turnstile” approach to transport are used to study the dynamics of the gyre. A Lagrangian recirculation boundary, consisting of pieces of stable and unstable manifolds joined by a gate, allows straightforward calculation and visualization of potential vorticity flux.

## 1. Introduction

Many types of recirculations are imbedded in the general circulation of the oceans and atmosphere. Some familiar examples are the subtropical ocean gyres, the stratospheric polar vortex, the inertial recirculations adjacent to the Gulf Stream, and topographically or coastally trapped eddies such as the “Great Whirl”, the Tsugaru gyre, and the Alboran gyre (Beal et al. 2000; Vindez et al. 1998; Nof and Pichevin 1999).

Attempts to understand recirculation cells often center on formulation of budgets of mass, vorticity, and other dynamical quantities for the cell as a whole. If the flow is time dependent, a boundary is typically defined by a closed streamline of a time-averaged flow and budgets are expressed in terms of fluxes of quantities across this fixed boundary. A well-known example is the Holland and Rhines (1980) analysis of an inertial recirculation imbedded in a two-layer, double-gyre ocean model. In their example the circulation is shown to be driven by eddy thickness and vorticity fluxes.

In some applications, it may be natural to define a

recirculation using a time varying boundary. Such is the case when the recirculation is not easily or helpfully described as a departure from a time mean or when one desires a budget that is continuous in time and follows the recirculation. It is convenient to make use of material (Lagrangian) contours (or surfaces), as this choice eliminates pseudofluxes created by movement of the recirculation as a whole past a fixed boundary. A choice motivated by dynamical systems theory is to construct a boundary by piecing together special material curves (or surfaces) called invariant manifolds. Such curves tend to distort and form filaments as time progresses, and eventually the boundary ceases to define a meaningful recirculation. This problem can be dealt with by regularly recomposing the boundary and, in essence, allowing material “lobes” to detach or be absorbed in the recirculation. Fluid lost or gained at the moment when the boundary is redefined is regarded as providing volume fluxes into and out of the recirculation. When the time dependence is periodic, the boundary so defined is also time periodic. The boundary redefinition is normally timed so that each outgoing lobe is compensated by an incoming lobe. The mass exchange thereby occurs as part of a “turnstile” mechanism (MacKay et al. 1984; Rom-Kedar and Wiggins 1990). “Lobe analysis” has been used to calculate the associated volume flux. Ex-

---

*Corresponding author address:* Patrick Miller, Department of Mathematical Sciences, Stevens Institute of Technology, Castle Point on Hudson, Hoboken, NJ 07030.  
E-mail: pmiller@stevens-tech.edu

amples of the use of this method include investigations of the wake cavities in the lee of cylinders (Shariff et al. 1992; Duan and Wiggins 1997), Hadley cells (Bowman and Cohen 1997), cat's eye recirculations in meandering jets (Samelson 1992; Duan and Wiggins 1996; Miller et al. 1996; Ngan and Shepherd 1997; Rogerson et al. 1999; Yuan et al. 2000, manuscript submitted to *J. Phys. Oceanogr.*, cellular circulations in Rossby wave fields (Malhotra and Wiggins 1998), and subtropical and subpolar ocean gyres (Poje and Haller 1999; Haller and Poje 1998; Coulliette and Wiggins 2000; Berloff et al. 2001, manuscript submitted to *J. Phys. Oceanogr.*). The analysis centers around the calculation of stable and unstable manifolds of hyperbolic trajectories that naturally arise in the Lagrangian description of many types of recirculations. The methods are described at various levels of rigor in the references just cited and in Wiggins (1992).

In addition to information about the rate of fluid exchange, lobe analysis provides a great deal of insight into stretching and folding processes that can cause stirring of physical properties around and within the recirculations. The investigator thereby gains detailed knowledge about eddy flux mechanisms that would be difficult to visualize in an Eulerian view of the flow field. However, only flow fields with relatively tame time dependence have been treated to date, for instance, periodic, quasiperiodic, or slowly varying. The work of Miller et al. (1997) and Rogerson et al. (1999) as well as the extension by Haller and Poje (1998) and Poje and Haller (1999) provide techniques for implementation in more general settings. However, it remains open as to how effectively the techniques can be implemented in flows that are far from steady or periodic.

Our investigation is centered on an analysis of a wind-forced recirculation trapped to the eastern boundary of an island in a simple model of wind-driven ocean circulation (Fig. 1a). One reason for choosing this particular example is that a steady, linear limit exists in which the properties of the recirculation can be determined analytically. By slowly increasing the forcing we can gradually induce time dependence leading to lobe transports. [On the other hand, the inertial gyre analyzed by Holland and Rhines (1980) is fundamentally nonlinear and requires a complete numerical description.] Previous studies have dealt with systems that, partly because of their divergence-free velocity fields, allow no sources of fluid exchange other than that due to the lobe mechanism. In our model, as in many oceanographic examples of interest, Ekman pumping through the top or bottom boundaries is present. Another reason for choosing the island setting is that this has been the subject of recent attention. Pedlosky et al. 1997, hereafter PPSH) showed recirculations to be common features of wind-driven,  $\beta$ -plane motion to the east of islands. In an abyssal ocean setting the island would be equivalent to a deep ridge segment and the wind stress curl would be represented by an equivalent upwelling velocity. As will be shown in the next section, the strength of the

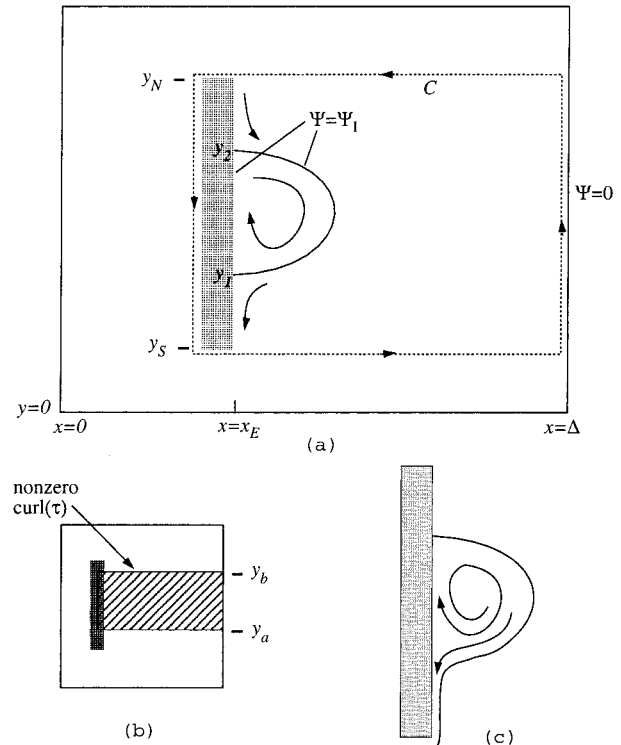


FIG. 1. Definition sketch (a) showing closed ocean basin containing an island with a recirculation gyre to the east. (b) The cross hatching shows the band in which the curl of the wind stress used in numerical calculations is nonzero. (c) The streak line patterns of a steady flow created when a small divergence of horizontal velocity is added due to downward Ekman pumping from above.

wind forcing is measured by the ratio of an inertial boundary layer thickness  $\delta_i$  to a viscous boundary layer thickness  $\delta_M$ . For weak forcing  $\delta_i/\delta_M$  is small and the circulation is steady and nearly closed. In this limit, there is a small leakage of mass due to surface Ekman pumping, leading to a weakly divergent flow as suggested in Fig. 1c. When  $\delta_i/\delta_M$  exceeds a value approximately equal to 1.8, an instability and ensuing unsteadiness sets in providing for a second source of fluid exchange, namely the lobe mechanism. The island setting is not at all a crucial element to our calculations: the underlying heteroclinic geometry of recirculations (such as the Alboran gyre or Great Whirl) trapped to continental boundaries is often the same.

The development of unsteadiness around the recirculation raises three questions that are relevant to the general issues outlined above. First, how rapidly does the volume exchange due to the time dependence (sometimes called the "lobe" or "chaotic" transport) increase relative to the Ekman transport? This is likely to be an issue for any type of recirculation that comes into contact with an Ekman layer, either surface or bottom. For a wind-driven, surface Ekman layer, we will show that the pumping increases in proportion to  $(\delta_i/\delta_M)^2$ . On the other hand, the volume flux associated with lobe trans-

port will be zero below the stability threshold  $\delta_I/\delta_M \approx 1.8$  but increases rapidly beyond that point. By performing a series of experiments with fixed  $\delta_M$  and increasing  $\delta_I$ , we will establish that above a value denoted by  $(\delta_I/\delta_M)_c$  the lobe transport clearly dominates the Ekman pumping (see Fig. 7 in section 3c, where the Ekman transport is given by the solid curve and the lobe transport by the dashed curve).

A second question can be raised concerning the fluxes of dynamical quantities associated with the above transports and their role in the maintenance of the recirculation. The most useful budget to consider in this regard is a form of Kelvin's circulation theorem<sup>1</sup> in which the recirculation is forced by the wind driving (whose vorticity input is transmitted down into the interior by Ekman pumping), retarded by viscous dissipation, and either forced or retarded by potential vorticity fluxes across the outer boundary due to waves and eddies. One of our aims is to compute this flux; another is to set up the calculation in a way that provides intuition through visualization of the flux. One idealization of the flux is that it takes place in lobes of fluid that enter and leave the recirculation while conserving potential vorticity. In such a regime, the net flux is due to a turnstile mechanism and can be calculated by subtracting the potential vorticity of incoming lobes from that of outgoing lobes. Past studies have not pursued this idealization, in part because the potential vorticity of fluid around the boundary is typically homogenized by the intense stretching and folding that occurs there. The net flux is therefore close to zero. Such models typically have weak forcing and dissipation. In our case, the potential vorticity in a given lobe constantly undergoes  $O(1)$  changes due to direct forcing by the wind or by diffusion into the island boundary. Different lobes have different potential vorticity. The presence of forcing and dissipative boundaries thus form something of a double edged sword for the potential vorticity flux calculation. On the one hand, fluid entering the recirculation generally has quite different potential vorticity than fluid leaving the recirculation, rendering the net flux levels more significant. On the other hand, the nonconservation of potential vorticity means that the idealization mentioned above is not an accurate picture of how the flux occurs. We attempt to deal with these issues by introducing an alternative Lagrangian boundary in which all mass exchange occurs through a narrow gate, allowing the flux to be measured and visualized. We will compare this calculation with something like a more traditional turnstile approach.

A final issue concerns the usefulness of the method of lobe dynamics in the presence of very strong and erratic time dependence, as occurs in the present model when

$(\delta_I/\delta_M)^2$  exceeds the stability threshold by a significant amount. Although stable and unstable manifolds can still be found and lobe transports formally calculated, it is less certain what one learns from the exercise. The problem hinges largely on one's ability to define a meaningful boundary for the recirculation and to deal with the excessive bookkeeping involved in keeping track of highly distorted lobes. Referring again to Fig. 7, we therefore expect that lobe analysis will be useful only within a window indicated by the shaded band. The object then is to determine the outer limit of the window.

Some of the advances laid out in the following pages involve methodology and will be of interest to dynamical systems specialists or to investigators hoping to apply the methods elsewhere. Others may be interested primarily in the physics of the recirculation, or circulation around islands, and may wish to avoid the considerable technical aspects of the methodology. The following is a road map that should make it easier for either to navigate the paper.

Section 2 reviews the linear theory for circulation around an island on a barotropic  $\beta$  plane. The conditions favorable for the formation of a recirculation are set down and the gyre geometry, dimensions, stability, and leakage are discussed. A numerical model is used to simulate the recirculation in the nonlinear regime. (All readers will want to understand this material.)

Section 3 begins with a brief presentation of the methods used for computing stable and unstable manifolds as they are applied to these aperiodic, finite-time flows. The discussion covers the concepts of hyperbolic regions and their effective invariant manifolds. For a more complete development of these methods the reader is referred to earlier publications (e.g., Miller et al. 1997; Haller and Poje 1998; Rogerson et al. 1999; Poje and Haller 1999). In section 3b we present a laboratory representation of the unsteady circulation with an example of an unstable manifold visualized using dye. Section 3c describes the results of the lobe analysis in terms of volume flux into and out of the recirculation relative to the leakage due to Ekman effects. It will be shown that the Ekman transport increases in proportion to  $(\delta_I/\delta_M)^2$  whereas the lobe exchange increases roughly in proportion to  $[(\delta_I/\delta_M)^2 - (1.8)^2]^{3.2}$ . Readers are encouraged to peruse the color diagrams showing the evolution of lobes in the strongly aperiodic flow field. The pictures give an idea of how mass enters and leaves the recirculation and its western boundary layer.

Section 4 discusses three attempts to gain dynamical information from the lobe analysis. Each involves the formulation of a vorticity budget in which the gyre is driven or damped by the wind stress curl and by the advective and diffusive fluxes of vorticity across the gyre boundary. The traditional approach, in which the boundary is defined by a closed streamline of the time-average flow, is compared with Lagrangian boundary formulations, the first of which computes advective fluxes as a lobe exchange mechanism and the second of

<sup>1</sup> The term circulation when used in connection with the term "circulation theorem" refers to the integral of the tangential velocity about a closed contour.

which forces the advective flux to occur through a gate. By their design, the Lagrangian formulations give the investigator more detailed information about how and where the fluxes occur. The ‘‘gate’’ approach turns out to be the most satisfying, although both Lagrangian approaches generally agree in terms of the sign and magnitude of the advective flux.

## 2. The linear recirculation

### a. Barotropic model

The calculations presented herein will be made using a model of depth-independent circulation driven by a body-force representation of wind stress. Although this model contains no explicit Ekman layers, the Ekman pumping rates for a surface wind stress equivalent to the prescribed body force can easily be calculated. Motion is governed by the shallow-water momentum equations for a homogeneous ocean:

$$\begin{aligned} \frac{\partial \mathbf{u}}{\partial t} + (\zeta + f)\mathbf{k} \times \mathbf{u} \\ = -\nabla \left( \frac{p}{\rho} + \frac{|\mathbf{u}|^2}{2} \right) + A_H \nabla^2 \mathbf{u} + \frac{\boldsymbol{\tau}}{\rho H}, \end{aligned} \quad (1)$$

where  $\mathbf{u} = (u, v)$  is the (depth independent) horizontal velocity,  $\zeta$  is the vertical component of vorticity ( $=\partial v/\partial x - \partial u/\partial y$ ),  $f$  is the Coriolis parameter,  $p$  is the (hydrostatic pressure),  $\rho$  is the density,  $A_H$  is the horizontal eddy viscosity, and  $\boldsymbol{\tau}/\rho$  represents the wind stress per unit mass. The ocean is assumed to have a horizontal lower boundary and an upper boundary that is free. Variations in the elevation of the latter will be small compared to the average total depth so that the actual depth  $H$  may be considered uniform. Also, the Coriolis parameter is assumed to vary linearly in the  $y$  direction:  $f = f_0 + \beta y$ . As shown in Fig. 1a, the ocean lies in a closed basin containing a rectangular island or ridge spanning a latitude band  $y_s < y < y_N$ .

Since  $\mathbf{u}$  is depth independent, a transport streamfunction  $\psi$  can be defined such that

$$uH = -\frac{\partial \psi}{\partial y} \quad \text{and} \quad vH = \frac{\partial \psi}{\partial x}, \quad (2)$$

where  $(u, v)$  are the eastward and westward ( $x$  and  $y$ ) velocity components. The vorticity equation for this system, obtained by taking the curl of (1) and use of (2), can be written as

$$\frac{d}{dt}(\zeta + \beta y) = \text{curl} \left( \frac{\boldsymbol{\tau}}{\rho H} \right) + \left( \frac{A_H}{H} \right) \nabla^4 \psi. \quad (3)$$

In the interior of the model ocean we anticipate a Sverdrup regime,  $\psi = \psi_s$ , in which (3) is approximated by

$$\beta \frac{\partial \psi_s}{\partial x} = \text{curl} \left( \frac{\boldsymbol{\tau}}{\rho H} \right). \quad (4)$$

The Sverdrup balance (4) may fail near lateral boundaries where boundary layers of two main types come into play. The first is the inertial layer of thickness  $\delta_I = (U/\beta)^{1/2}$ , where  $U$  is a velocity scale based on the Sverdrup balance (4). The second is the Munk layer, which occurs only on western (east facing) boundaries and has the thickness  $\delta_M = (A_H/\beta)^{1/3}$ . A boundary layer Reynolds number

$$\frac{U\delta_M}{A_H} = \left( \frac{\delta_I}{\delta_M} \right)^2 \quad (5)$$

provides a measure of the importance of relative vorticity advection in comparison with dissipation within a western boundary layer. In the present study we shall explore values of  $\delta_I/\delta_M$  ranging from  $\ll 1$  (for which the boundary layer is linear and frictionally dominated) to values just over 2. Instability and subsequent unsteadiness [probably due to something like the Munk layer instability discussed by Ierley and Young (1991)] is observed beyond  $\delta_I/\delta_M \approx 1.8$ .

Now suppose that an  $x$ -independent wind stress  $\boldsymbol{\tau} = \boldsymbol{\tau}(y)$  is imposed and  $\delta_I/\delta_M \ll 1$  so that the circulation is steady and linear in the ocean interior and in western boundary layers. One can solve for the circulation in the usual manner by first integrating the Sverdrup relation from the eastern basin boundary ( $x = \Delta$ ) to a point  $x$  in the interior. In doing so, the condition of no normal flow through the eastern basin boundary is imposed by assuming that  $\psi_s = 0$  there. This procedure results in

$$\psi_s(x, y) = (x - \Delta)\beta^{-1} \text{curl}(\boldsymbol{\tau}(y)/\rho). \quad (6)$$

If  $y$  lies in the latitude range  $y_s < y < y_N$  of the island, (6) is valid right up to the outer edge  $x = x_E + O(\delta_M)$  of the Munk layer on the eastern side of the island. Within the Munk layer  $0 < x - x_E < O(\delta_M)$  the streamfunction  $\psi$  departs from  $\psi_s$  as determined by bringing the viscous terms back into play (e.g., Pedlosky 1996). To construct a boundary layer solution for  $\psi$  that satisfies the conditions of no normal flow and no slip at  $x = x_E$ , the value of the streamfunction  $\psi_I$  on the island boundary must be determined. Under linear conditions, this value is provided by the Island Rule (Godfrey 1989):

$$\psi_I = \frac{-\oint_C (\boldsymbol{\tau}/\rho) \cdot \mathbf{t} \, ds}{\beta(y_N - y_s)}, \quad (7)$$

obtained by integrating the tangential component of (1) about the contour  $C$  shown in Fig. 1a. Numerical tests by PPSH have shown that (7) remains robust<sup>2</sup>

<sup>2</sup> In a series of numerical simulations based on the Munk model, and with various island shapes and forcing, the island rule is generally found to overestimate the actual  $\psi_I$  by a modest 0–25%. In addition, it is found that the overestimate is primarily due to the presence of friction acting along the north and south boundaries of the island and, to a lesser extent, the west coast of the island and the east coast of the basin. Other possible sources of error, such as net relative vorticity fluxes due to eddy shedding, boundary layer separation, and other nonlinear processes are found to be of secondary importance.

even when the boundary layer dynamics becomes inertial [ $\delta_I/\delta_M = O(1)$ ].

### b. The recirculation

We are now in a position to lay out the conditions favorable to the formation of a recirculation on the east coast of the island. As suggested in Fig. 1, this coast will contain a “western” boundary layer. The northern and southern extents of the recirculation along the coast will correspond to separation points of the boundary layer. Since the net meridional transport in the boundary layer at a particular  $y$  is given by the difference between the Sverdrup streamfunction at the outer edge of the boundary layer  $\psi_S(x_E + \delta_M, y)$  and  $\psi_I$  and since  $\psi_S(x_E + \delta_M, y) \equiv \psi_S(x_E, y)$ , separation occurs at those  $y$  such that  $\psi_S(x_E, y) = \psi_I$ . A recirculation requires two such

points, and since  $\psi_S(x_E, y) = (x_E - \Delta)\beta^{-1} \text{curl} [\boldsymbol{\tau}(y)/\rho]$ , a necessary (though not sufficient) condition for the recirculation to exist is that the curl of the wind stress reaches an extreme value within  $y_S < y < y_N$ . Since the boundary of the recirculation is defined by the streamline  $\psi = \psi_I$ , the eastern boundary  $x = x_c$  of the recirculation at any  $y$  can be calculated by setting  $\psi_S[x_c(y), y] = \psi_I$ , or

$$\beta^{-1}(x_c(y) - \Delta) \text{curl} (\boldsymbol{\tau}(y)/\rho) = \psi_I \quad (8)$$

in view of (6). The latitudes  $y_1$  and  $y_2$  of the separation (or stagnation) points are therefore given by  $(x_E - \Delta)\beta^{-1} \text{curl} [\boldsymbol{\tau}(y_{1,2})/\rho] = \psi_I$ , while the maximum eastern extent of the recirculation is given by the maximum value of  $\Delta + \beta\psi_I/\text{curl} (\boldsymbol{\tau}(y)/\rho)$  in  $y_S \leq y \leq y_N$ .

As an example, consider the zonal wind stress  $\boldsymbol{\tau} = (\tau^x, 0)$

$$\tau^x = \begin{cases} \tau_0, & y_b \leq y, & x \geq x_\tau \\ \frac{\tau_0}{2} \left[ 1 + \cos\left(\frac{\pi(y_b - y)}{y_b - y_a}\right) \right], & y_a \leq y \leq y_b, & x \geq x_\tau \\ 0, & \text{otherwise} \end{cases} \quad (9)$$

over a basin 2000 km wide by 2000 km long by 1000 m deep containing a rectangular island extending from  $y_S = 420$  km to  $y_N = 1600$  km. The wind stress curl is nonzero only within the band  $y_a = 800$  km to  $y_b = 1400$  km, with  $x \geq x_\tau = 1000$  km as suggested in Fig. 1b. We take  $\tau_0 > 0$  so that the wind stress curl is negative over this band, reaching a minimum value at the central latitude  $y = 1000$  km. The linearity of the corresponding solution is measured by  $\delta_I/\delta_M$  in which the velocity scale  $U$  in  $\delta_I = (U/\beta)^{1/2}$  is calculated from the Sverdrup relation (6) as applied to the wind stress (9). By this measure

$$\left(\frac{\delta_I}{\delta_M}\right)^2 = \frac{\tau_0}{\rho\beta^{4/3}H(y_1 - y_2)A_H^{2/3}}. \quad (10)$$

Figure 2 shows the steady circulation calculated numerically using the full shallow-water equations with the setting  $\delta_I/\delta_M = 1.0$  and the Munk layer thickness fixed at 40 km. In the Sverdrup interior to the east of the island the meridional velocity is southward. Most of this interior fluid flows in a circuit that circumscribes the island and winds its way through a variety of boundary layers. To the immediate east of the island exists the expected recirculation. The stagnation point ( $x = x_E, y_2 = 1324$  km) marking the northwestern corner of the recirculation is marked by the convergence of two western boundary layers, one from the north (carrying fluid that has circulated around the island) and one from the south (carrying

fluid trapped within the recirculation). The southern stagnation point ( $x = x_E, y_1 = 861$  km) marks diverging western boundary layers. The eastern boundary of the recirculation extends well into the Sverdrup interior to the east of the island.

All numerical solutions presented herein have been computed using the Miami Isopycnic Coordinate Ocean Model (MICOM) documented by Bleck et al. (1992). Flow fields are spun up from rest to a steady or statistically steady state, a process taking 500–1000 days. The barotropic version of the MICOM model solves for the free surface height and there is no need to independently specify the pressure on the island. Thus  $\psi_I$  is determined without direct reference to the island rule or any related integral constraints. In addition the grid spacing and Munk layer thickness are fixed at 20 km and 40 km, respectively, so that the frictional boundary layers are well resolved. Tests of numerical accuracy against a linear, analytical solution were performed by PPSH (see their section 5iii) and agreement with the predicted  $\psi_I$  within 1% was found for sufficiently small  $\delta_I/\delta_M$ .

### c. Mechanisms for leakage from the recirculation

By regarding  $\boldsymbol{\tau}$  as a depth-independent body force in (1) we have avoided a three-dimensional aspect of the circulation that comes into play when  $\boldsymbol{\tau}$  is imposed at the upper surface. In the more realistic case an Ekman layer of thickness  $\delta_E = (2A_v/f_0)^{1/2}$ , where  $A_v$  is the

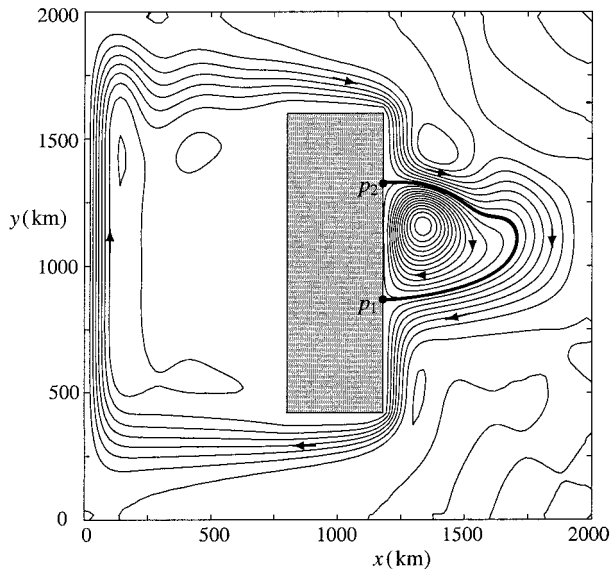


FIG. 2. The steady circulation as calculated numerically using the full shallow-water equations with the strongly linear setting  $\delta_l/\delta_M = 1.0$  and the Munk layer thickness fixed at 40 km.

vertical eddy viscosity, forms at the surface. Motion in the inviscid interior region below the Ekman layer is forced by a vertical “pumping velocity”  $w_E = \text{curl}(\tau/\rho f_0)$  through the base of the Ekman layer. If  $L_c$  denotes the characteristic horizontal length scale of the recirculation gyre, then the total volume flux pumped down into the gyre is  $L_c^2$  times the average  $w_E$  over the recirculation. According to the Sverdrup balance, the total recirculating volume transport in the gyre is approximately the Sverdrup velocity  $(BH)^{-1} \text{curl}(\tau/\rho)$  multiplied by  $HL_c$ . The ratio of the Ekman transport to the Sverdrup transport is therefore  $O(\beta L_c/f_0)$ , which is  $\ll 1$  in the standard  $\beta$ -plane approximation. The horizontal circulations produced by the two models are nondivergent and identical to this order of approximation. Nonetheless, it is interesting to ask what happens to the extra mass flux pumped downward into the gyre when a surface Ekman layer is present. Although the potential leakage from the recirculation is small, it represents the only mechanism for material transport between the gyre and its surroundings when the flow is steady.

There are several possible answers to the above question. First, the extra mass may be accepted into a bottom Ekman layer and, from there, removed from the recirculation laterally. However, for realistic wind stresses the surface Ekman pumping far exceeds the volume flux that can be accepted into the bottom Ekman layer. The inviscid interior region must therefore assimilate most of the downwelled fluid. The second possibility is that the extra mass is upwelled along the island boundary [as described by Pedlosky (1987, sec. 4.13)] and returned to the surface Ekman layer. However this situation would require a wind stress component parallel to the island boundary, a feature absent in the present sit-

uation. The remaining possibility is that the fluid is carried out of the recirculation in the inviscid interior; that is, the recirculation is not closed. If the horizontal streamline pattern from Figs. 1a or 2 is corrected to account for the secondary flow, the streakline pattern that emerges looks something like that drawn in Fig. 1c. PPSH present an example showing how this correction is calculated. For our purposes, it is only necessary to observe that the “leakage” out of the original recirculation is proportional to  $\tau_0$  and therefore to  $\delta_l^2$  [see Eq. (10)]. We will perform a series of calculations in which  $\delta_M$  remains fixed at 40 km and for which we may therefore regard the Ekman leakage being proportional to  $(\delta_l/\delta_M)^2$ . By direct calculation using the linear solution for the wind stress distribution (9), the volume leakage rate (also the volume Ekman pumping transport over the gyre) is given by  $T_E \cong 0.1 (\delta_l/\delta_M)^2 \text{ Sv}$  ( $\text{Sv} \cong 10^6 \text{ m}^3 \text{ s}^{-1}$ ).

If the wind stress, and therefore the value of  $\delta_l$ , is increased, the western boundary layer on the island will become unstable and leakage into and out of the recirculation can occur as a result of the time-dependent effects alluded to in the introduction. This process is discussed next.

### 3. Mass transport across the recirculation boundary

The theory of chaotic advection offers an effective method for assessing transport across active flow regions. In time-dependent horizontal flow fields the tangling of stable and unstable manifolds of certain distinguished stagnation, or periodic, points in the field creates a zone in which parcel motion is chaotic. Another view of this same scenario is that the stable and unstable manifolds delineate regions of distinguished dynamic fate and their tangling marks off regions of fluid that switch from one flow regime to another, so-called fluid exchange. This technique has led to the theory of lobe dynamics and chaotic transport (MacKay et al. 1984; Rom-Kedar and Wiggins; Wiggins 1992).

The use of stable and unstable manifolds as orchestrating fluid exchange, in this way, requires the presence of a saddle-type stagnation or fixed point in the flow field. In this recirculation problem, as  $\delta_l/\delta_M$  is increased and the time dependence of the flow becomes stronger, such fixed points cannot be expected to occur. However, the key local properties of stretching and compressing in complementary directions, called hyperbolicity, can still be present to an extent that affords an analogous theory. While lobe dynamics has been extended to the aperiodic case (Malhotra and Wiggins 1998), the flow fields under consideration here persist over only finite spans of time and theories based on the usual asymptotic conditions are not directly applicable.

The key observation is that, although no distinguished hyperbolic stagnation points will be present, distinguished invariant manifolds akin to the stable and un-

stable manifolds of fixed points are present in even quite complicated flow fields. This theory was first developed in Miller et al. (1997) and Rogerson et al. (1999) and depends on isolating localized regions, rather than points, where there is strong hyperbolicity over the time interval of interest. Based on the dynamics in such a region, *effective* invariant manifolds can be generated in a fashion entirely analogous to the case where hyperbolic fixed points, or trajectories, are present. As viewed in the  $x$ - $y$  plane, these manifolds are just time slices of distinguished material surfaces in  $x$ - $y$ - $t$  space. They are pinned by the hyperbolic regions and supply transport templates as in the periodic case. The hyperbolic regions are found near critical points of the frozen-time Eulerian field (see Haller and Poje 1998). In the simulations presented here, such hyperbolic regions can be found near where the boundary of the gyre meets the island. Under appropriate conditions, the manifolds are then defined to within a certain measurable uncertainty (Haller and Poje 1998).

The numerical computation of the manifolds then proceeds as follows. An initial line segment is placed in the identified hyperbolic region (for now, we denote this region by  $\gamma$ ). The initial segment should *straddle* the hyperbolic region at  $t = t_0$  so that the endpoints move apart under the evolution of the flow field (this requires aligning the segment with the “unstable” directions). Iterating the line segment forward in time determines an approximate finite-time unstable manifold for this hyperbolic region, denoted  $W^u(\gamma)$ . Because the manifold stretches rapidly it is necessary to insert additional trajectories at intermediate times to keep the curve sufficiently resolved. By construction, all the points on this manifold return to the hyperbolic region as  $t$  decreases to  $t_0$ . Computing the stable manifold  $W^s$  associated with a hyperbolic region  $\gamma$  requires running the flow backward in time starting from some later time  $t_1 > t_0$ . This manifold will be created by propagating an initial line segment that straddles the hyperbolic region along the “stable” direction at  $t = t_1$ .

#### a. Stable and unstable manifolds for the recirculation

In the flows being investigated here, the boundary used to characterize Lagrangian transport into and out of the recirculation gyre is associated with a heteroclinic structure connecting two hyperbolic regions of the flow along the eastern boundary of the island. When the flow is steady (see Fig. 2 for  $\delta_I/\delta_M = 1.0$ ) the recirculation boundary is just the contour of the transport streamfunction at  $\psi = \psi_I$ , the value of  $\psi$  at the island boundary. All points on the island boundary are necessarily fixed points because of the no-slip boundary conditions. The distinguished points where the recirculation boundary meets the island satisfy  $v_x = 0$ , with  $v_{xy} > 0$  at the southern attachment point ( $p_1$ ) and  $v_{xy} < 0$  at the northern point ( $p_2$ ). The linearization at  $p_1$  (respectively  $p_2$ ) has a zero eigenvalue in the direction tangent to the

island boundary and one stable (respectively unstable) eigenvalue.

For larger values of  $\delta_I/\delta_M$ , where the velocity field is time dependent, the transport will be characterized by the transverse intersections of finite-time stable and unstable manifolds, denoted  $W_1^s = W^s(\gamma_1)$  and  $W_2^u = W^u(\gamma_2)$ . The hyperbolic trajectory near the southern end of the island boundary  $\gamma_1$  is still defined on the boundary of the island in the region where the flow separates into fluid flowing to the north and fluid flowing to the south. The manifold  $W_1^s$  is computed numerically by initializing a segment of initial points at time  $t = 100$  days and evolving this curve backward in time to  $t = 0$ . The initial line segment has one end connected to the island boundary and is directed orthogonally to the boundary. The Lagrangian trajectories are computed using a fourth-order Runge–Kutta solver to integrate the numerical velocity field output from the MICOM package. The initial time  $t = 0$  used in the dynamical systems analysis corresponds to 1500 days in the numerical solution of the shallow-water equations. The calculation of  $W_1^s$  for the case  $\delta_I/\delta_M = 2.25$  is shown in Fig. 3a.<sup>3</sup> Here the stable manifold is shown at  $t = 30$  days, after integrating the velocity for 70 days. Numerical experiments using different locations and different orientations for the initial data showed negligible differences in the global manifold, consistent with the estimates in Haller and Poje (1998).

When the velocity field is time dependent, there appears a small eddylike structure along the boundary of the island just to the north of the main recirculation (labeled  $S$  in Fig. 3a). While the flow in this region is quite slow and does not exchange much fluid with the surrounding flow, it does have the effect that the second hyperbolic trajectory  $\gamma_2$  is no longer on the boundary of the island. Numerical experiments show that the recirculation boundary emanates from a region approximately 2–4 grid points (40–80 km) off the island boundary where the flow coming from the north (passing around the corner of the island) separates from the boundary layer. It is important to note that the location of this second hyperbolic region is really borne out by the pattern of the tangle formed by  $W_1^s$  after long integration times (see Fig. 3a). The tangles are clearly accumulating some distance from the island boundary implying that the crucial hyperbolic trajectory must also be in this region, modulo some uncertainty in the initialization of  $W_2^u$ . The initialization for  $W_2^u$  is a line segment aligned orthogonal to the island boundary and chosen to straddle the heteroclinic tangle formed by the stable manifold  $W_1^s$ . The calculation of  $W_2^u$  for  $\delta_I/\delta_M = 2.25$  is shown in Fig. 3b at  $t = 70$  days. Again, comparisons from a number of different initializations shows insignificant differences in the eventual transport calculations. Of interest in section 3c will be the principal

<sup>3</sup> Note that in the figures the distinguished hyperbolic trajectories are labeled as  $p_i$  rather than  $\gamma_i(t)$ .

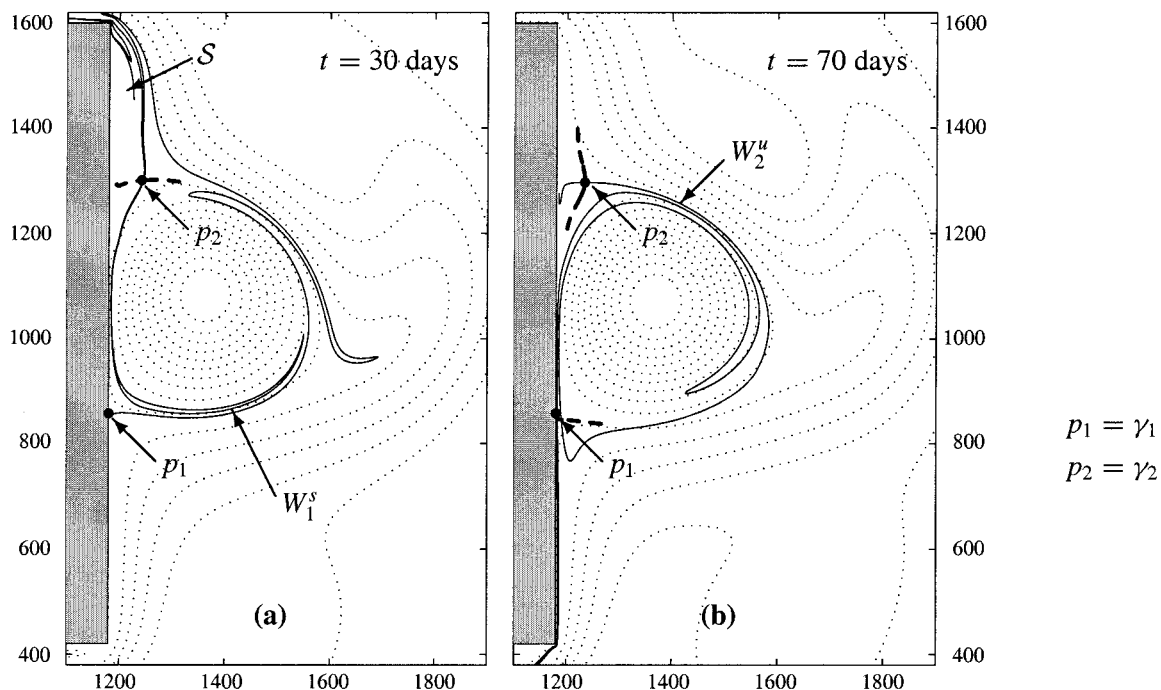


FIG. 3. For  $\delta_i = 90$  km ( $\delta_i/\delta_M = 2.25$ ), the (a) stable manifold  $W_1^s$  at  $t = 30$  days and (b) the unstable manifold  $W_2^u$  at  $t = 70$  days. The distinguished hyperbolic trajectories are denoted  $p_1$  and  $p_2$ . In (a) note how the heteroclinic tangle that forms in the vicinity of  $p_2$  is accumulating some distance from the island boundary. Here the heavy dashed line is a short segment of  $W_2^s$ . In (b) the dashed lines are segments of the stable manifolds  $W_1^s$  and  $W_2^s$ . The dotted lines are level contours of the transport streamfunction.

intersections<sup>4</sup> between  $W_1^s$  and  $W_2^u$  and the resulting lobes that form as the regions bounded by the segments of stable and unstable manifolds connecting adjacent intersection points.

*b. A laboratory example*

Before discussing the results from the numerical model it is useful to see a laboratory demonstration of the unstable manifold and associated transport across the mean island recirculation cell boundary (Fig. 4). The laboratory apparatus is the lid-driven sliced cylinder analogue of wind-driven circulation in a  $\beta$ -plane basin described in detail in PPSH. The laboratory tank contains a thin north–south oriented island that spans 0.85 times the tank diameter (41.5 cm). The flow is driven by a spatially uniform downward Ekman pumping with  $\delta_i/\delta_M \approx 2.3$ . Figure 4 shows a sequence of closeup video images from a camera looking down onto the experiment, with north to the top of the image. In the images the horizontal stripe near the top of each frame is a thin needle used to deliver neutrally buoyant dye to visualize the flow. The dye is injected just north of the recirculation zone on the eastern boundary of the island (the

wide vertical stripe). It then flows southward to the northern intersection point  $p_2$  from where it moves into the interior to define the unstable manifold. The sequence shows clearly the growing meanders characteristic of the unstable manifold and the subsequent folding of the meanders as the southern intersection point is approached. The exchange of fluid across the mean recirculation zone boundary is illustrated by the filaments that are brought into the recirculation cell [frames (c)–(d)] and subsequently stirred within the recirculation zone [frames (e)–(f)]. Fluid initially inside the cell is squeezed out in the lower lobe in frames (c)–(f).

*c. Mass transport via lobe analysis*

In this section we summarize the mass transport calculations for the four parameter cases,  $\delta_i = 85, 90, 95,$  and  $100$  km. In all cases the Munk layer thickness is fixed at  $\delta_M = 40$  km so that  $2.125 \leq \delta_i/\delta_M \leq 2.50$ . The mass transport will be relative to a dynamic, Lagrangian recirculation boundary consisting of segments of stable and unstable manifolds, as described previously.

In the following description of the mass transport calculations, we refer the reader to Fig. 5 showing snapshots of the manifolds and lobes for  $\delta_i/\delta_M = 2.375$ , at times  $t = 25, 35, 67, 68$  days. To define a Lagrangian boundary for the recirculation gyre, it is helpful to first label the principal intersection points  $q_0, q_1, \dots$ , where the ordering is chosen such that  $q_0$  is the pip nearest

<sup>4</sup> For an intersection  $q$ , let  $W^u[p_1, q]$  denote the segment of  $W_1^u$  extending from  $p_1$  to  $q$  and  $W^s[q, p_2]$  the segment of  $W_2^s$  extending from  $q$  to  $p_2$ . If  $W^u[p_1, q]$  and  $W^s[q, p_2]$  intersect only at  $q$  we say that  $q$  is a principal intersection point or pip (see Wiggins 1992).

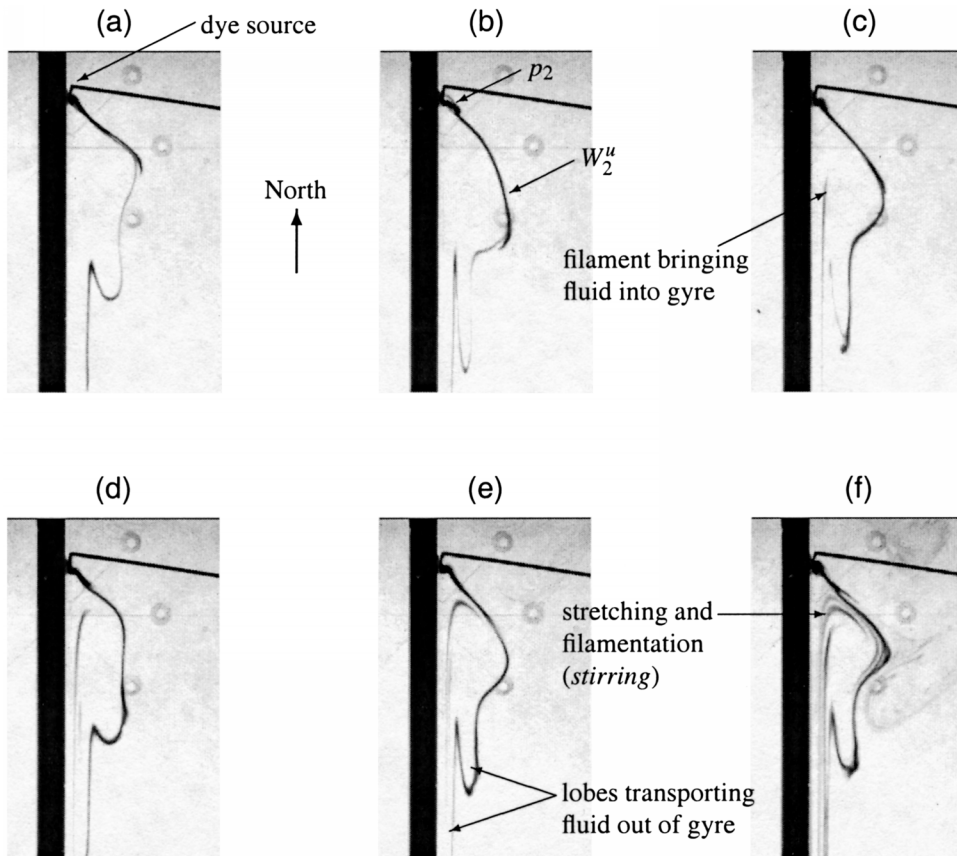


FIG. 4. A sequence of video images showing the unstable manifold from a laboratory experiment with  $\delta_l/\delta_M \approx 2.3$ . Time increases from (a) to (f). The island width is 1.2 cm.

the hyperbolic point  $p_1$  as measured along its stable manifold  $W_1^s$ . As a means of marking events the horizontal line  $y = 1050$  km is chosen as a fixed reference point since this section divides the gyre in more or less equal north and south parts. All of the pips must cross this reference line as they move clockwise around the gyre so let  $t_i$  denote the first time the intersection point  $q_i$  lies below this reference line. The first *turnstile event* begins at  $t = t_0$ , the time at which the first pip  $q_0$  crosses the reference line, and extends to  $t = t_2$ , the point at which the first two lobes have crossed the reference line. More generally, the  $k$ th turnstile event covers the time interval  $[t_{2k-2}, t_{2k}]$ . For the time interval  $t_{2k-2} \leq t < t_{2k}$ , the boundary is defined as  $W_1^s[p_1, q_{2k-2}] \cup W_2^u[q_{2k-2}, p_2]$ . At time  $t_{2k}$  the boundary is redefined as  $W_1^s[p_1, q_{2k}] \cup W_2^u[q_{2k}, p_2]$  and the next pair of lobes enter the turnstile, beginning a new turnstile event. The times  $t_0, t_2, \dots$  will be referred to as the *turnstile times*. In Fig. 5 the first two frames show the manifolds at the start of the first and second turnstile events, respectively. The last two frames show the contorted shape of the recirculation boundary near the end of the second turnstile interval ( $t = 67$ ) and its more symmetric shape just after starting the third turnstile interval ( $t = 68$ ).

Let  $A_k$  denote the lobes transporting mass from outside to inside the gyre and  $B_k$  the lobes carrying fluid from inside to outside. Then the  $k$ th turnstile event consists of the two lobes  $A_k$  and  $B_k$  with  $A_k$  outside the recirculation and  $B_k$  inside the recirculation for  $t_{2k-2} \leq t < t_{2k}$ . At time  $t_{2k}$  when the boundaries are redefined the lobes cross into the opposite regions and there has been an exchange of mass between the two regions. Figure 6 compares the shape and size of the lobes at  $t = 50$  days for all four parameter cases. In Fig. 6 the chaotic transport  $T_C$  is computed by summing the area from each of the  $B_k$ , multiplying by a depth of 1000 m, and dividing by the total time covered by the sequence of turnstile events. The results are expressed in Sverdrups and also presented as a graph in Fig. 7. The solid curve represents the Ekman transport estimated by integrating curl  $(\tau/\rho f_0)$  over the area of the recirculation as defined by the linear theory. The ovals are the chaotic transport calculations just described. The dashed curve is the result of a least squares fit to  $T_C = c_1[(\delta_l/\delta_M)^2 - (1.8)^2]^{n_1}$ , yielding  $c_1 = 0.54$  and  $n_1 = 3.2$ . The critical value at which chaotic transport overtakes the Ekman pumping is then estimated as  $(\delta_l/\delta_M)_c \approx 1.96$ .

Table 1 lists the transport for all four parameter cases

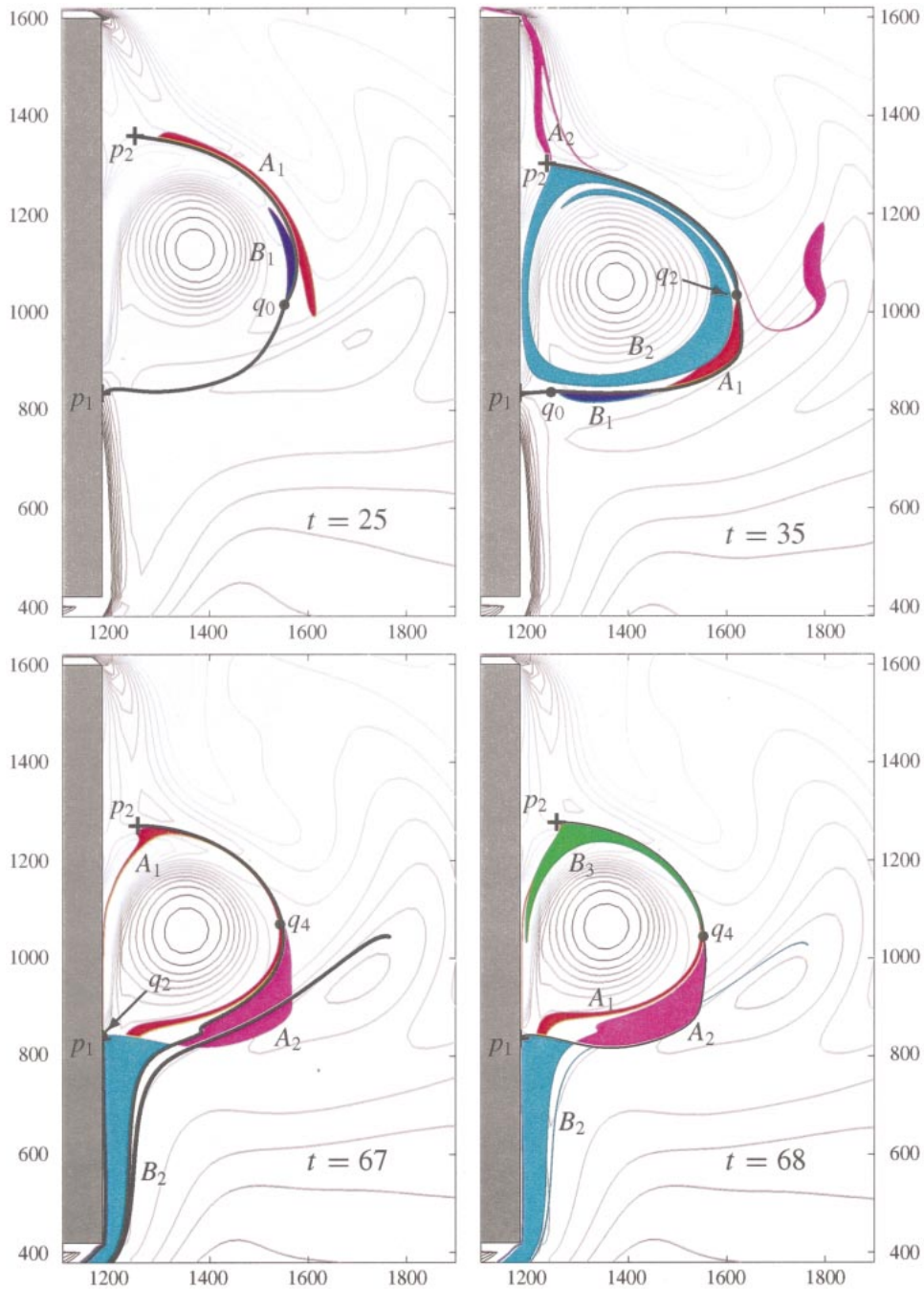


FIG. 5. Boundary and turnstile dynamics for  $\delta_i = 95\text{km}$  ( $\delta_i/\delta_M = 2.375$ ). At  $t = 25$  days, the start of the first turnstile period, lobe  $A_1$  is outside the gyre and  $B_1$  is inside. At  $t = 35$ , the boundary has been redefined by switching from pip  $q_0$  to pip  $q_2$ . Now lobe  $A_1$  is inside the gyre and  $B_1$  is outside and the new turnstile is made up of lobes  $A_2$  and  $B_2$ . Because of the larger turnstile lobes and longer time interval, the gyre boundary is greatly distorted near the end of the second turnstile period. The gyre returns to a more symmetric shape at  $t = 68$  when the boundary is redefined using pip  $q_4$ . Note that  $A_2$  is now inside and  $B_2$  outside the gyre.

broken down by each turnstile event identified in the dynamical systems analysis. Here the transports are calculated for each turnstile period by taking the volume of fluid in the lobe and dividing by the length of the

time interval for the appropriate turnstile event. Note the irregular pattern in the lobe areas and transport calculations from one period to the next.

Figure 8 shows the lobe evolution for the parameter

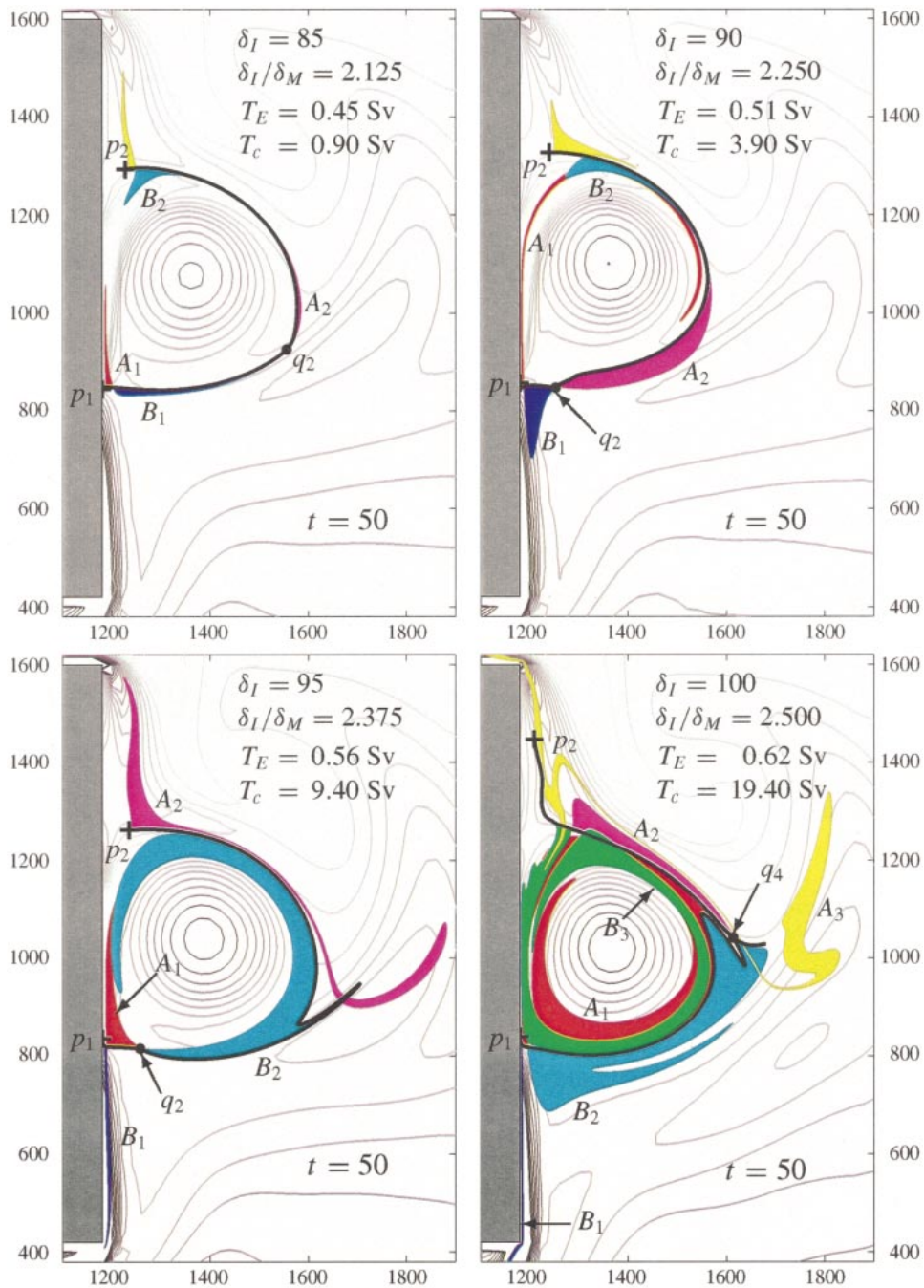


FIG. 6. Summary of the chaotic transport calculations at four values of  $\delta_I/\delta_M$ :  $T_E$  denotes the leakage due to Ekman pumping and  $T_C$  quantifies the fluid exchange associated with lobe dynamics.  $T_C$  is calculated as the total volume of fluid entering the gyre (sum of the positive values in Table 1) divided by the total interval of time covered by the turnstile events. These results are also plotted in Fig. 7.

value  $\delta_I = 100$  km. This analysis captures three complete turnstile events covering  $t = 13$  through  $t = 81$  days. Inspection of Figs. 5, 6, and 8 shows that fluid entering the gyre originates from two regions: the western boundary layer approaching from the north and the Sverdrup interior to the east. These sources are clearly illustrated by the evolution of lobe  $A_2$  of Fig. 5 between

$t = 35$  and  $t = 68$ . At  $t = 35$  the (magenta) lobe has extensions into the western boundary layer to the north of the gyre and into the Sverdrup interior to the east. At  $t = 68$  the lobe has coalesced into a less contorted blob lying inside the gyre. Similar behavior is demonstrated by lobes  $A_1$  and  $A_3$  of Fig. 8. A second feature worth noting is that fluid drawn into the gyre flows into

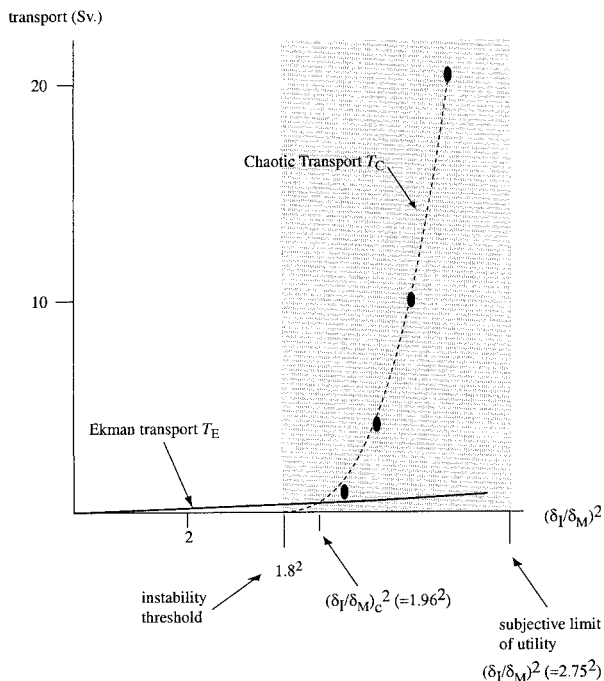


FIG. 7. Ekman transport (solid line) vs transport due to chaotic advection (dashed line). The dashed curve corresponds to (25), which is an approximate fit to the numerically determined transports indicated by the ovals and listed in Fig. 6 (also see Table 1). The Ekman transport  $T_E$  is equal to the downward Ekman pumping velocity integrated over the fixed area of the recirculation as determined by linear theory. Note that  $T_E$  is independent of  $\delta_M$  and is regarded here as a function of  $\delta_l/\delta_M$  only insofar as  $\delta_M$  is fixed in the numerical experiments. The shaded area indicates the range in  $\delta_l/\delta_M$  over which the method of lobe dynamics and the Lagrangian definition of the recirculation boundary is applicable and helpful.

the (northward) western boundary current in the gyre interior and is eventually wrapped around the periphery (see the red lobes labeled  $A_1$  in each of these figures). In no case does the chaotic transport penetrate into the very center of the gyre.

**4. Potential vorticity budget for the recirculation**

The dynamics of the gyre can be characterized using a vorticity budget in which circulation is forced by the wind stress curl, damped by viscous diffusion of potential vorticity ( $q = \zeta + \beta y$ ) into the island and either damped or driven by diffusive and advective potential vorticity fluxes across the free boundary. The gyre can be described as having an inertial character when the advective potential vorticity flux  $F_q$  is as large as the wind forcing, otherwise the gyre is dominated by the same linear dynamics as described in section 2. It is natural to think of  $F_q$  as being due to the turnstile mechanism since this accounts for nearly all of the material exchange between the gyre and its surroundings. If lobe fluid conserved  $q$  while entering and leaving the gyre,  $F_q$  would equal the difference in area-integrated  $q$  be-

TABLE 1. Summary of the mass transport for each of the four parameter cases. Lobes labeled  $A_i$  transport fluid into the Lagrangian recirculation at the end of the turnstile interval, the  $B_i$ 's carry fluid out of the recirculation. In comparing these to the color figures in this section, the lobes are colored as follows:  $A_1$  red,  $B_1$  blue,  $A_2$  magenta,  $B_2$  cyan,  $A_3$  yellow,  $B_3$  green. The mass transport is calculated by multiplying the lobe area by a depth of 1000 m and dividing by the length of the turnstile interval. The transport is recorded in Sverdrups and time in days.

Time interval	Lobe	Transport	$\delta_l/\delta_M$
[21, 43]	$A_1$	0.667	2.125
	$B_1$	-1.209	
[43, 66]	$A_2$	0.756	2.250
	$B_2$	-1.095	
[18, 35]	$A_1$	3.658	2.375
[35, 58]	$B_1$	-2.992	
[25, 35]	$A_2$	6.714	2.500
	$B_2$	-1.905	
[35, 68]	$A_1$	8.408	2.500
	$B_1$	-3.161	
[13, 36]	$A_2$	5.990	2.500
	$B_2$	-14.912	
[36, 59]	$A_1$	33.556	2.500
[59, 81]	$B_1$	-18.806	
[36, 59]	$A_2$	4.914	2.500
	$B_2$	-19.346	
[59, 81]	$A_3$	19.812	2.500
	$B_3$	-19.724	

tween incoming and outgoing lobes divided by the turnstile time interval. In fact,  $q$  is altered by the wind forcing and by diffusion, the latter being particularly strong near the island boundary. Despite the presence of strong wind forcing in these simulations, there is still a remarkable correlation between the lobes and the strongest changes in potential vorticity as measured along Lagrangian trajectories. As we show next, the fluid contained in lobes experiences some of the swiftest  $q$  changes of all the fluid in the basin. Another way to express this is to say that curves associated with the *strongest gradients* of the field that measures the change in  $q$  are in close correspondence with the effective invariant manifolds.

Let  $\mathbf{x}(t; t_0, \mathbf{x}_0)$  denote the trajectory at time  $t$  with initial condition  $\mathbf{x}(t_0) = \mathbf{x}_0$ , and  $q(t, \mathbf{x})$  the potential vorticity,  $q = \zeta + \beta y$ . For a fixed initial time  $t_0$  and final time  $t_f$ , define a scalar field, the *Lagrangian potential vorticity change*,  $\delta_q(\mathbf{x}_0; t_0, t_f)$ , which gives the increase in potential vorticity along a trajectory emanating from the initial point  $\mathbf{x}_0$  at time  $t_0$ , up to a fixed time  $t_f$ :

$$\delta_q(\mathbf{x}_0; t_0, t_f) = q[t_f, \mathbf{x}(t_f; t_0, \mathbf{x}_0)] - q(t_0, \mathbf{x}_0). \quad (11)$$

Figure 9 shows  $\delta_q$  for  $\delta_l = 95$  km and initial times  $t_0 = 50$  and  $t_0 = 70$ . In both cases a grid of initial conditions covering the region of the recirculation is run forward and backward for 30 days. The function  $\delta_q(\mathbf{x}_0; t_0, t_f)$  is plotted against  $W_1^2(t_0)$  when  $t_f > t_0$  and against  $W_2^2(t_0)$  when  $t_f < t_0$ . Note that some of the strongest changes in  $q$ , as indicated by deep reds and blues, occur

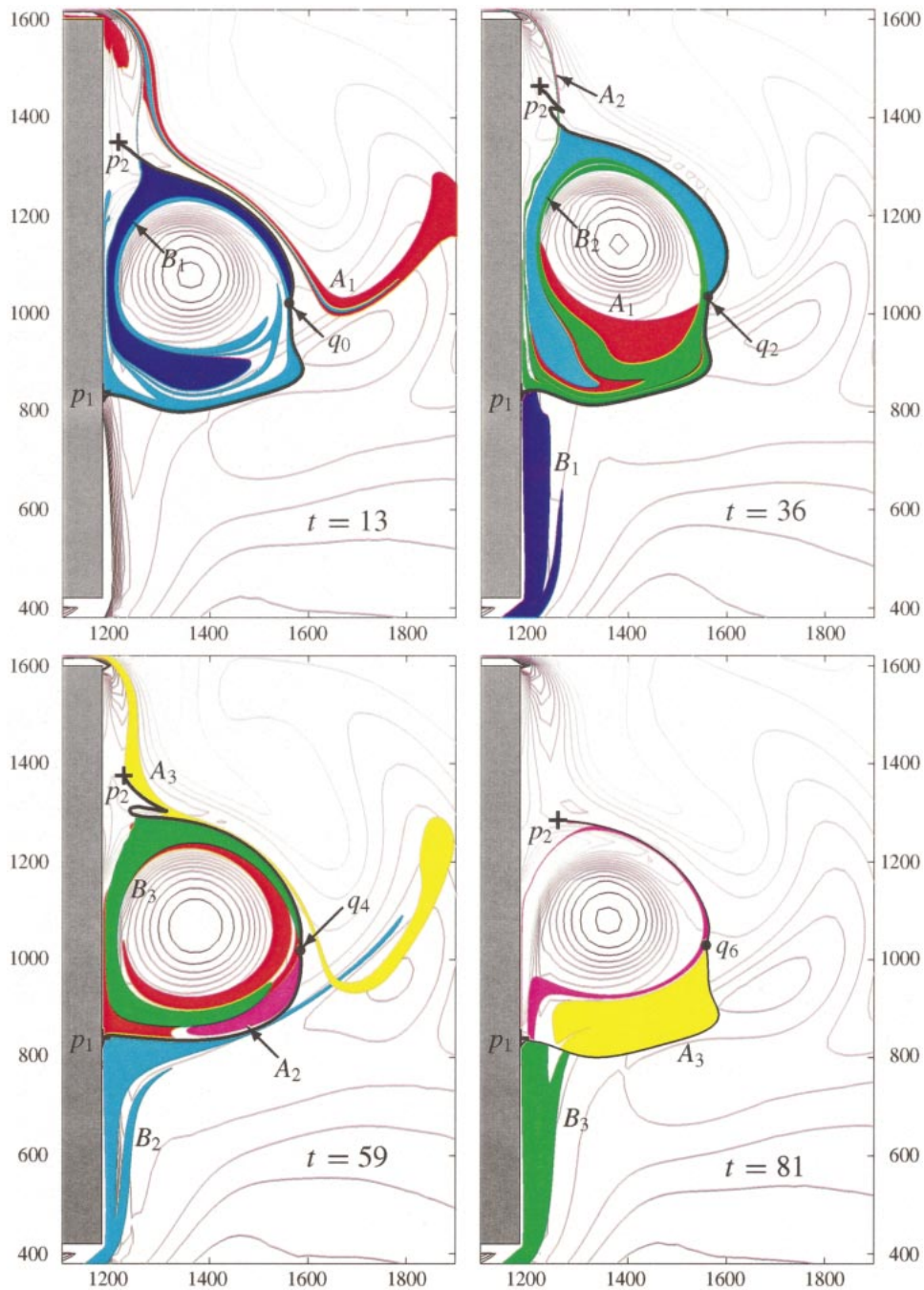


FIG. 8. Lobe dynamics for  $\delta_r = 100\text{km}$  ( $\delta_r/\delta_M = 2.50$ ). The lobes are shown at the start of each new turnstile event. Lobes  $A_1$ ,  $A_2$ , and  $A_3$  bring fluid into the recirculation,  $B_1$ ,  $B_2$ , and  $B_3$  carry fluid out of the gyre. At  $t = 36$  most of lobe  $A_2$  is still out of view above the northern boundary of the island.

in fluid contained in lobes. Two examples, both in the first frame, are the thin red lobe located in the Sverdrup interior just to the east of the circulation and the larger, dark blue lobe extending around the northern edge of the recirculation in the same frame. Not all lobes experience strong changes, but the strongest changes are often associated with lobes.

It is not surprising that lobes experience preferentially large changes in  $q$ . As Figs. 5, 6, and 8 suggest, lobes entering the recirculation are rapidly stretched into filaments that extend through the western boundary current. Much of the material contained in lobes leaving the recirculation also begins in the western boundary current. Even without the aid of the dissipative island

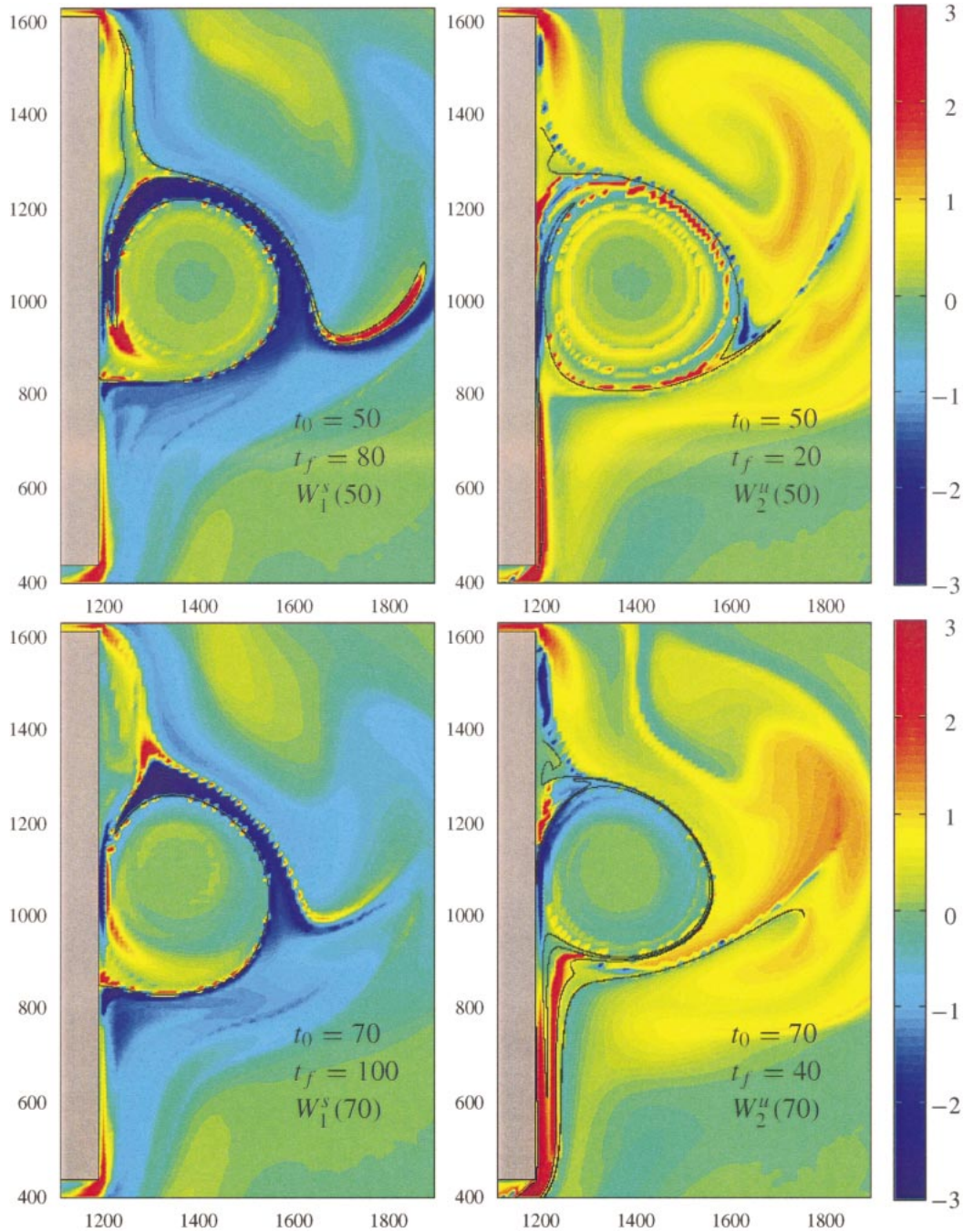


FIG. 9. Plots of the scalar field  $\delta_s(\mathbf{x}_0; t_0, t_f)$  as defined in (11), for the case  $\delta_r = 95$  km ( $\delta_r/\delta_M = 2.375$ ). The initial and final times,  $t_0$  and  $t_f$ , are indicated in each figure. For  $t_f > t_0$  the stable manifold  $W_1^s(t_0)$  is overlaid on the 2D plot. For  $t_f < t_0$  the unstable manifold  $W_2^u(t_0)$  is overlaid.

boundary, the stretching and folding of material contours associated with hyperbolic regions will tend to enhance potential vorticity diffusion, an effect demonstrated by Rogerson et al. (1999). Clearly, advective potential vorticity flux is not simply a matter of blobs of different potential vorticity passing through a turn-

stile. However, it is possible to formulate the vorticity budget in which the advective flux occurs entirely through a gate between  $W_1^s$  and  $W_2^u$ , allowing unambiguous interpretation and visualization. We will describe this approach and compare it to the traditional method of using a fixed boundary and to a modified version of

the turnstile. Each approach is based on an integrated form of (3), restated here in terms of the velocity field  $\mathbf{u}$  rather than the transport streamfunction  $\psi$ :

$$\frac{d}{dt}(\zeta + \beta y) = \text{curl}\left(\frac{\boldsymbol{\tau}}{\rho H}\right) + A_H \text{curl}(\nabla^2 \mathbf{u}). \quad (12)$$

We approximate the depth  $H$  as uniform and therefore,  $\nabla \cdot \mathbf{u} = 0$ . Let  $Q(R, t)$  denote the total potential vorticity integrated over a region  $R(t)$  with boundary  $\partial R$ . Thus,

$$\begin{aligned} Q(R, t) &= \iint_{R(t)} q(x, y, t) dx dy = \iint_{R(t)} (\zeta + \beta y) dx dy \\ &= \Gamma - \frac{\beta}{2} \oint_{\partial R} y^2 \mathbf{i} \cdot \mathbf{t} ds, \end{aligned} \quad (13)$$

where  $\Gamma = \oint_{\partial R} \mathbf{u} \cdot \mathbf{t} ds$  is the circulation about the closed contour  $\partial R$  and  $\mathbf{t}$  is the unit tangent vector in the counterclockwise direction.

#### a. Time-averaged recirculation

The traditional characterization of the potential vorticity fluxes for the recirculation region involves defining an appropriate time-averaged recirculation region and calculating the contributions to  $dQ/dt$  due to wind forcing, advective fluxes across the boundary, and dissipation. To identify an average recirculation region, the velocity field is time averaged over the interval of 100 days and the closed streamline  $\psi = \psi_l$  of the time-average flow is used to define the boundary of the recirculation zone denoted  $R_0$ . Integration of (12) over the region enclosed by this boundary yields the following expression for  $dQ/dt$ ,

$$\begin{aligned} \frac{dQ}{dt} &= \iint_{R_0} \frac{\partial q}{\partial t} dx dy \\ &= \iint_{R_0} \left( -\mathbf{u} \cdot \nabla q + \frac{\nabla \times \boldsymbol{\tau}}{\rho H} + A_H \nabla \times \nabla^2 \mathbf{u} \right) dx dy. \end{aligned} \quad (14)$$

Converting the right-hand side to appropriate contour integrals yields

$$\begin{aligned} \frac{dQ}{dt} &= \oint_{\partial R_0} -q \mathbf{u} \cdot \mathbf{n} ds + \oint_{\partial R_0} \frac{\boldsymbol{\tau} \cdot \mathbf{t} ds}{\rho H} \\ &\quad + A_H \oint_{\partial R_0} \nabla^2 \mathbf{u} \cdot \mathbf{t} ds, \end{aligned} \quad (15)$$

where again the direction of integration is assumed to be counterclockwise. The right-hand side terms in (15) can be interpreted as sources and sinks of potential vorticity for the gyre. Since the gyre boundary is fixed,

(13) implies that  $dQ/dt = d\Gamma/dt$ , and thus the sources or sinks of potential vorticity act to strengthen or weaken the circulation  $\Gamma$  of the gyre.

In the following discussion it will be helpful to use a simpler notation for each of the terms appearing in (14) and (15), namely,

$$Q'(R_0, t) = Q'_A(R_0, t) + Q'_S(R_0, t) + Q'_D(R_0, t). \quad (16)$$

The objective is to compare the relative sizes of each of the three terms on the right-hand side. The quantity  $Q'(R_0, t)$  is determined by first calculating  $Q(R_0, t)$  from (13) and then numerically differentiating the time series. The advective flux  $Q'_A(R_0, t)$  and the contribution from the wind stress  $Q'_S(R_0, t)$  are computed directly from the velocity, potential vorticity, and wind fields. The value of the dissipative term  $Q'_D(R_0, t)$  is implied by requiring Eq. (15) to balance.

Results for all four parameter cases are presented in Fig. 10, including plots for each of the four terms in Eq. (16). The timescales are chosen to match the time intervals used in section 4c. For  $\delta_l = 85$  km the budget is dominated by  $Q'_S(R_0)$  and  $Q'_D(R_0, t)$ , implying that the gyre is driven by the wind and damped by diffusion of vorticity across its boundary (primarily across the island boundary). As  $\delta_l$  increases, the advection of potential vorticity  $Q'_A(R_0, t)$  becomes more significant, even exceeding  $Q'_S$  for a time interval in the  $\delta_l = 100$  case. We will later show that this apparently inertial character of the gyre is simply due to the motion of the gyre vortex as a whole back and forth across the time-average boundary.

#### b. Potential vorticity advection using lobes

Now consider characterizing the potential vorticity budget for the recirculation using the Lagrangian boundary as defined in section 3c. Except for the discrete set of times when the recirculation boundary is redefined, this boundary is material and therefore permits no advective transport into the recirculation. For almost all  $t$ , Eq. (15) is replaced by

$$\begin{aligned} \frac{dQ}{dt} &= \iint_{R(t)} \frac{d}{dt}(\zeta + \beta y) dx dy \\ &= \oint_{\partial R(t)} \frac{\boldsymbol{\tau} \cdot \mathbf{t} ds}{\rho H} + A_H \oint_{\partial R(t)} \nabla^2 \mathbf{u} \cdot \mathbf{t} ds. \end{aligned} \quad (17)$$

Using this description of the recirculation region, transport can only take place at the discrete times chosen to redefine the Lagrangian boundary. For potential vorticity transport we choose to characterize the change in  $Q(R, t)$  at each of the pip times,  $t_0, t_1, \dots$ , denoting the times that the principal intersection points  $q_0, q_1, \dots$  cross the reference line  $y = 1050$  km. The  $k$ th lobe crosses the reference line during the time interval,  $t_{k-1} \leq t < t_k$ . The increase in potential vorticity  $Q(R, t)$  over this time interval is the quantity,

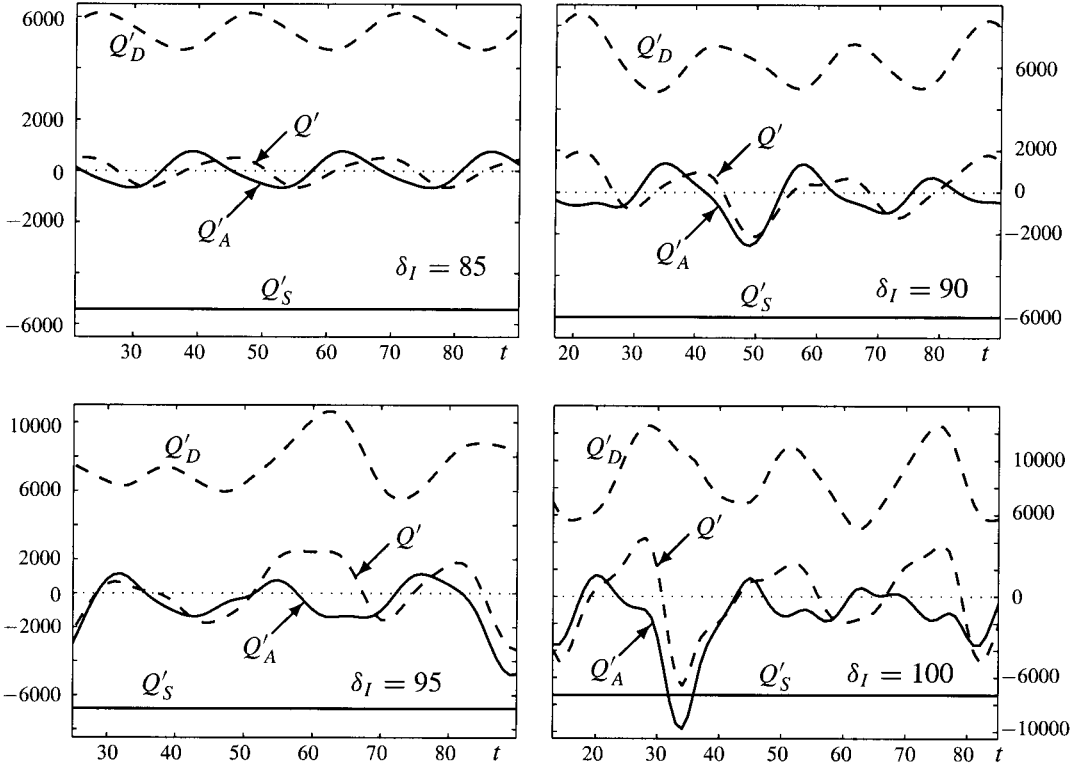


FIG. 10. Potential vorticity budget using a fixed boundary  $\partial R_0$  based on the time-averaged flow. The vertical scale for  $Q'$  is in units of  $\text{cm}^2 \text{sec}^{-2}$ . The four curves in each plot satisfy the equation  $Q' = Q'_A + Q'_S + Q'_D$ .

$$\Delta_k Q(R) = Q(R, t_k^+) - Q(R, t_{k-1}^+). \quad (18)$$

This change in potential vorticity can be expressed as the sum of two terms,

$$\Delta_k Q(R) = [Q(R, t_k^+) - Q(R, t_k^-)] + [Q(R, t_k^-) - Q(R, t_{k-1}^+)]. \quad (19)$$

The second pair of terms on the right-hand side contain all nonadvective changes in  $Q(R, t)$  that take place over the time interval  $t_{k-1} \leq t < t_k$ . The first pair of terms, which we shall denote  $\Delta_k Q(L)$ , measures the increase in  $Q(R, t)$  due to the redefinition of the boundary at time  $t_k$ :

$$\Delta_k Q(R) = \Delta_k Q(L) + [Q(R, t_k^-) - Q(R, t_{k-1}^+)]. \quad (20)$$

If the boundary redefinition is thought of as a rapid but continuous movement of  $\partial R$  from one position to another, then  $\Delta_k Q(L)$  results from *apparent* advection due to a moving boundary passing through essentially stationary potential vorticity. The same interpretation applies to mass flux calculations involving the turnstile mechanism. In practice,  $\Delta_k Q(L)$  is simply computed as the potential vorticity in lobe  $L_k$  that finishes crossing the reference line at time  $t_k$ . If this lobe is carrying fluid from outside to inside the gyre, the contribution from advection is  $\Delta_k Q(L) = Q(L_k, t_k)$ . If the lobe is carrying fluid from inside to outside, the change in  $Q(R)$  due to advection is  $\Delta_k Q(L) = -Q(L_k, t_k)$ . These calculations

are summarized in Table 2 for each of the four parameter cases. In section 4d, the results tabulated here will be compared with the integral of  $Q'_A$  as computed in sections 4a and 4c.

Note that if the turnstile times  $t_0, t_2, \dots$  are used to characterize potential vorticity transport, as was done for mass transport, the results vary considerably due to the long turnstile intervals and the irregular pattern of the turnstile times. The quantity  $Q(L)$  can vary considerably over the period of a turnstile interval and the transport calculations are very sensitive to how the turnstile lobes are defined. Calculating the change in potential vorticity after each lobe crossing (i.e., one lobe at a time) shortens the time intervals and the results are found to be in much better agreement with the calculations using a gate in section 4c.

### c. Potential vorticity advection using a gate

The third approach combines a Lagrangian description of the recirculation gyre with a mechanism for describing the advective fluxes continuously in time. The boundary of the gyre will be defined using segments of stable and unstable manifolds joined by a nonmaterial surface, referred to as the gate. This is based on the methods used in Poje and Haller (1999) to describe transport and mixing in eddies where the finite-time

TABLE 2. Summary of the potential vorticity transport as calculated at each of the pip times:  $\Delta_k Q(L)$  is expressed in units of  $10^9 \text{ cm}^2 \text{ s}^{-1}$ , time is in units of days.

$k$	Time	$\Delta_k Q(L)$	$\delta_l/\delta_M$
0	$t_0 = 21$		2.125
1	$t_1 = 32$	0.023	
2	$t_2 = 43$	-0.033	
3	$t_3 = 56$	0.019	
4	$t_4 = 66$	-0.035	
5	$t_5 = 79$	0.022	
0	$t_0 = 18$		2.250
1	$t_1 = 29$	0.054	
2	$t_2 = 35$	-0.172	
3	$t_3 = 52$	-0.097	
4	$t_4 = 58$	-0.144	
5	$t_5 = 71$	0.004	
0	$t_0 = 25$		2.375
1	$t_1 = 27$	-0.097	
2	$t_2 = 35$	0.103	
3	$t_3 = 54$	-0.936	
4	$t_4 = 68$	-0.203	
5	$t_5 = 79$	-0.154	
0	$t_0 = 13$		2.500
1	$t_1 = 27$	0.090	
2	$t_2 = 36$	-1.108	
3	$t_3 = 50$	-0.273	
6	$t_6 = 59$	0.083	
7	$t_7 = 70$	-0.630	
10	$t_{10} = 81$	-0.873	

stable and unstable manifolds did not intersect transversely.

Referring the reader to Fig. 11, a reference line  $\mathcal{G}$  is chosen at  $y = 1050 \text{ km}$  (to coincide with the reference line used in identifying the turnstile events). Moving along the stable manifold  $W_1^s$  from where it begins at  $p_1$ , the first intersection with  $\mathcal{G}$  is identified as  $s_1$ . Similarly, moving along  $W_2^u$  starting at  $p_2$ , the first intersection with  $\mathcal{G}$  is labeled  $u_1$ . Then the gate is just the segment of  $\mathcal{G}$  joining these two points,  $\mathcal{G}[s_1, u_1]$ , and the boundary of the recirculation  $R_g(t)$  is defined as the union of five curves,

$$\partial R_g = W_1^s[p_1, s_1] \cup \mathcal{G}[s_1, u_1] \cup W_2^u[u_1, p_2] \cup B_2 \cup B_1. \quad (21)$$

The first term on the right-hand side of (21) is the segment of stable manifold connecting  $p_1$  with  $s_1$ , the second term is the gate, and the third term is the segment of unstable manifold joining  $u_2$  to the distinguished trajectory  $p_2$ . The last two pieces are necessary to close the boundary:  $B_2$  is the horizontal line segment connecting  $p_2$  with the island boundary, and  $B_1$  is the section of the island boundary returning back to the point  $p_1$ .

For this definition of the recirculation  $R_g(t)$ , the equation for  $dQ/dt$  becomes

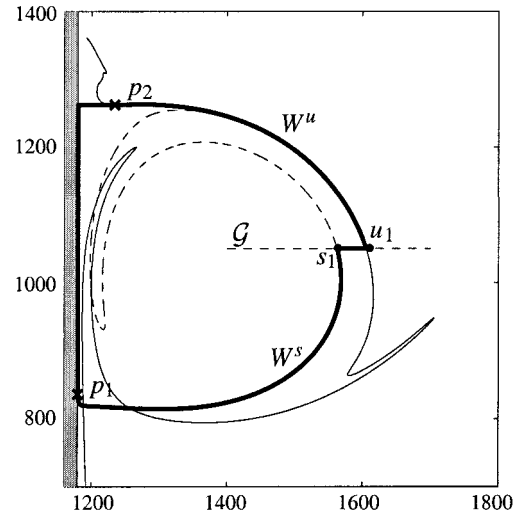


FIG. 11. Illustration of the recirculation boundary as defined using the gate  $\mathcal{G}[s_1, u_1]$ . This figure shows the recirculation for the case  $\delta_l = 95 \text{ km}$  ( $\delta_l/\delta_M = 2.375$ ) at time  $t = 50$  days.

$$\frac{dQ}{dt} = Q'(R_g, t) = - \int_{s_1}^{u_1} q \mathbf{u} \cdot \mathbf{n} ds + \oint_{\partial R_g(t)} \frac{\boldsymbol{\tau} \cdot \mathbf{t}}{\rho H} ds + A_H \oint_{\partial R_g(t)} \nabla^2 \mathbf{u} \cdot \mathbf{t} ds. \quad (22)$$

The first term on the right-hand side is the advective flux<sup>5</sup>  $Q'_A$ , the second term is  $Q'_S$ , and the third term  $Q'_D$ , just as in (16).

While this gate technique can still produce discontinuities in the definition of the boundary (see the appendix), the method does yield a nearly continuous Lagrangian description of the recirculation gyre and a straightforward characterization of fluxes. The potential vorticity budget described in (22) is plotted in Fig. 12 for each of the four parameter cases. Each plot includes the four terms,  $Q'$ ,  $Q'_S$ ,  $Q'_D$ , and  $Q'_A = - \int_{s_1}^{u_1} q \mathbf{u} \cdot \mathbf{n} ds$ . Comparing these plots with the results for the static boundary in Fig. 10, it is clear that the range of values for the advective term  $Q'_A$  is considerably smaller for the Lagrangian recirculation.

#### d. Comparisons

As a means of comparing the continuous descriptions of potential vorticity advection with the turnstile description of advection in section 4b, it is useful to consider the cumulative change in  $Q(R, t)$  attributable to advection. The continuous advective terms,  $Q'_A(R_0, t)$  and  $Q'_A(R_g, t)$ , are integrated over  $t$ , starting at the initial turnstile time  $t_0$ :

<sup>5</sup> Since the velocities are quite small in the vicinity of the boundary  $B_2$ , any advective fluxes across  $B_2$  are negligible compared with the fluxes across the gate.

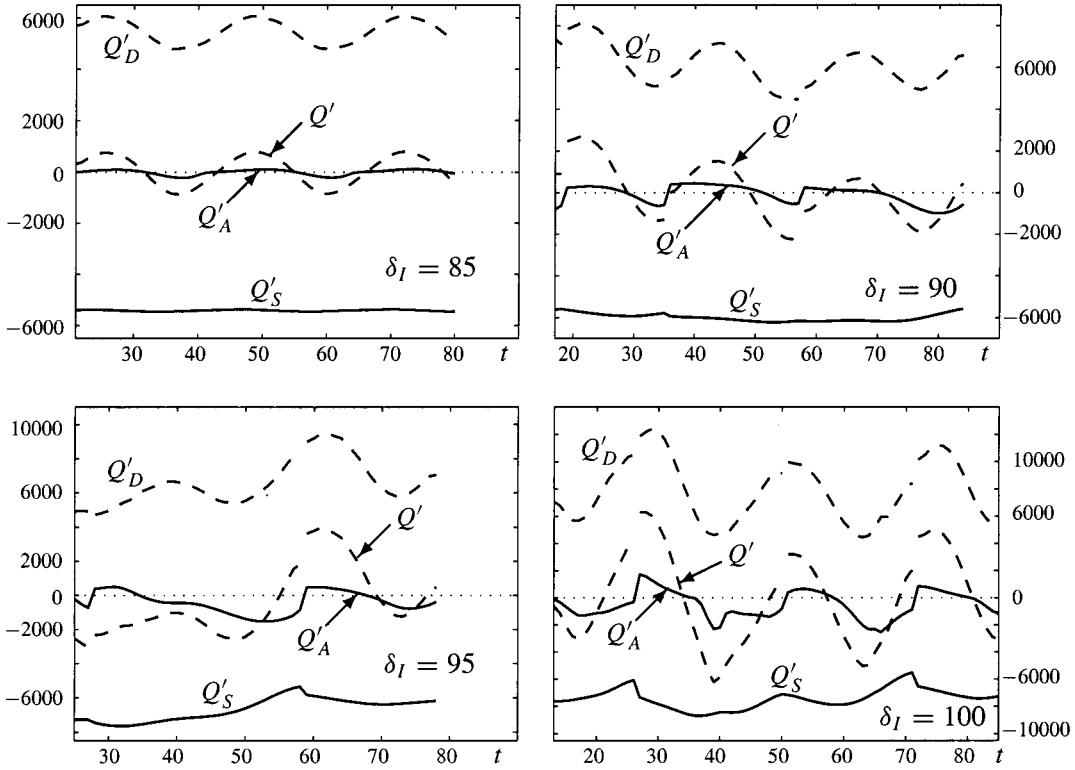


FIG. 12. Potential vorticity budget for the recirculation  $R_g$  defined using the gate  $\mathcal{G}$ . The vertical scale for  $Q'$  is in units of  $\text{cm}^2 \text{sec}^{-2}$ . The three terms  $Q'$ ,  $Q'_S$ , and  $Q'_D$  are calculated using the boundary defined with  $\mathcal{G}[s_1, u_1]$ . The advective flux  $Q'_A$  is calculated by the methods described in section 4c.

$$\Delta Q(t; t_0) = \int_{t_0}^t Q'_A(\xi) d\xi. \quad (23)$$

The discrete transport calculations described in section 4b are summed up over the turnstile times,

$$\Delta Q(t_N; t_0) = \sum_{k=1}^N \Delta_k Q(L),$$

for  $N = 1, 2, \dots$  and  $\Delta Q(t_0; t_0) = 0,$

(24)

where the values for  $\Delta_k Q(L)$  are taken from Table 2. The time  $t_0$ , the point at which the principal intersection point  $q_0$  crosses the reference line  $\mathcal{G}$ , is also the first time for which the gate flux  $Q'_A(R_g, t)$  is defined. The results of these calculations are plotted in Fig. 13. The dotted line in each of the four plots is the linear interpolation of the discrete transport numbers defined in (24).

The potential vorticity budgets plotted in Figs. 10 and 12 confirm that defining the recirculation from a time-averaged velocity field consistently yields artificially large values for the advective flux  $Q'_A$ , as compared with  $Q'_A$  for the Lagrangian description of the recirculation. Much of this large variation in  $Q'_A(R_0, t)$  can be attributed to the large-scale motion of the Lagrangian

boundary. The most significant effect is likely due to the fluctuations in the location of  $W_2^u$  near the northernmost boundary of the recirculation. Figure 14 shows two snapshots of the Lagrangian boundary  $\partial R_g$  overlaid on the fixed boundary  $\partial R_0$  illustrating the variability in the location of the Lagrangian boundary. In particular, note the motion of the northern boundary defined by  $W_2^u$ , which results in a significant mass transport across  $\partial R_0$  though these fluid particles are neither entering nor leaving the Lagrangian recirculation.

The two Lagrangian methods show similar trends<sup>6</sup> though the gate method shows a greater variability as the lobes alternate between incoming and outgoing fluxes. This can be explained by the fact that as lobe  $L_k$  is crossing the gate, the quantity  $Q(L_k, t)$  is usually decreasing with  $t$ . At time  $t_k$  where  $Q(L_k, t_k)$  is used to estimate the advective increase in  $Q(R)$ , most of the fluid particles are at a lower potential vorticity than at the time where they crossed the gate, resulting in smaller fluctuations in  $Q(R)$  than that determined from the gate. The biggest discrepancy between the two Lagrangian methods appears in the case  $\delta_I = 90$ , but even this difference is due largely to just one lobe event. The

<sup>6</sup> Least squares fits show that the potential vorticity flux for the gate increases in proportion to  $[(\delta_I/\delta_M)^2 - (1.8)^2]^{2.6}$ , whereas the lobe flux increases like  $[(\delta_I/\delta_M)^2 - (1.8)^2]^{3.2}$ .

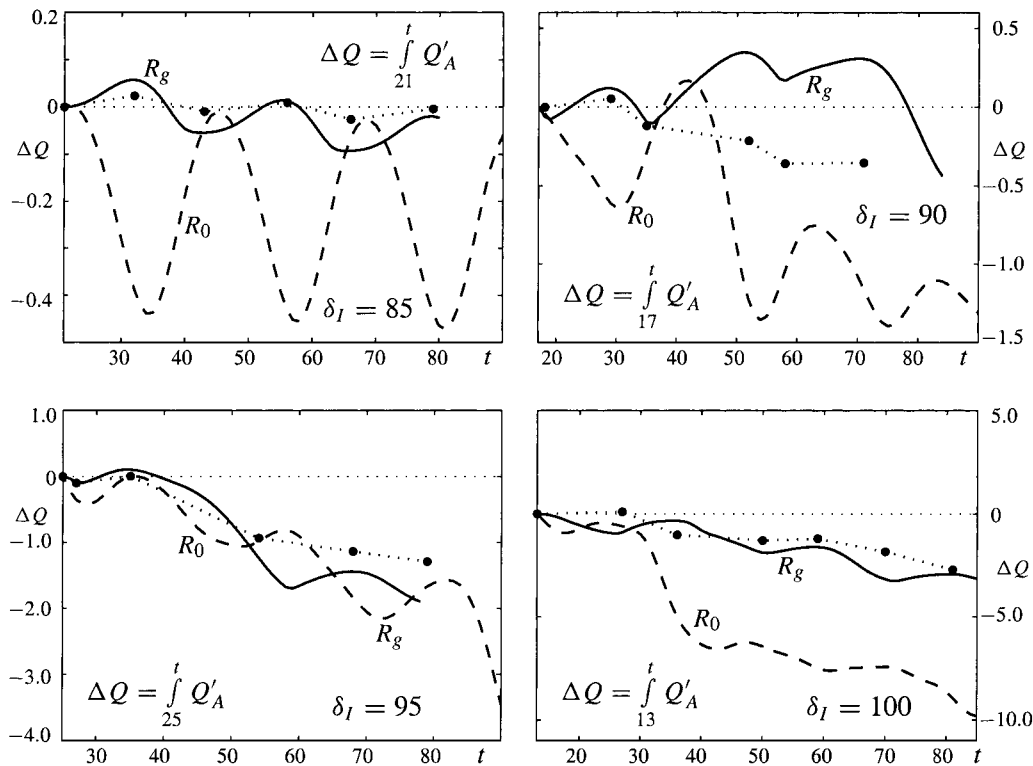


FIG. 13. The cumulative change in potential vorticity associated with advective fluxes at the boundary of the recirculation. The continuous cases,  $\Delta Q = \int_{t_0}^t Q'_A(R, \xi) d\xi$ , are denoted by  $R_0$  and  $R_g$ . The dotted line is an interpolation of the discrete case from section 4b and Table 2,  $\Delta Q = \sum_k \Delta_k Q(L)$ . The initial time  $t_0$  used in the integration coincides with the start of the first turnstile event. All curves are plotted in units of  $10^9 \text{ cm}^2 \text{ s}^{-1}$ .

third lobe, a lobe carrying fluid into the recirculation  $R_g$ , takes a much longer time to cross the gate ( $35 \leq t \leq 52$ ) and  $Q(L_3)$  has decreased considerably by the time the change in potential vorticity is recorded at  $t = 52$ . In addition to being easier to calculate, the gate method appears to provide the least ambiguous estimates for advective fluxes relative to a Lagrangian description of the recirculation, particularly when quantifying fluxes over short time intervals.

## 5. Discussion and summary

We now return to the three fundamental issues raised at the beginning of this work. First, how rapidly does the lobe (or chaotic) volume transport  $T_C$  compare to the Ekman transport  $T_E$  out of the recirculation? The dashed curve in Fig. 7, which corresponds to

$$T_C = 0.54[\delta_I/\delta_M]^2 - (1.8)^2]^{3/2}, \quad (25)$$

gives a least squares fit to the computed values indicated by ovals. The lobe transport thus grows much more rapidly than the Ekman transport beyond the instability threshold value  $\delta_I/\delta_M \approx 1.8$ . The two transports are roughly equal at  $\delta_I/\delta_M \approx 1.96$ , but chaotic advection dominates for larger values. The lobe diagrams (Figs. 5, 6, and 8) show that the chaotic transport process

draws fluid into the gyre from the western boundary layer to the north and from a particular region of the Sverdrup interior to the east. Fluid is ejected into the western boundary layer to the south of the recirculation. The chaotic transport fills the edges of the recirculation but does not penetrate to the middle. Two cautionary remarks should be made. First,  $T_E$  represents a net flux out of the recirculation whereas  $T_C$  represents an exchange rate. Second,  $T_E$  is independent of  $\delta_M$  and is only regarded here as a function of  $\delta_I/\delta_M$  for the purposes of comparison in a series of experiments for which  $\delta_M$  is fixed. Changing the value of  $\delta_M$  could therefore shift the value of  $(\delta_I/\delta_M)_c$  given above, but the property of rapid growth and dominance of the chaotic advection process is likely generic.

The second issue was whether lobe analysis can provide insight into the dynamics of the recirculation. Our analysis has focused on differences in the potential vorticity budget that arise from Eulerian and Lagrangian definitions of the recirculation boundary. The (traditional) Eulerian approach uses a closed streamline of the time-averaged flow to define the boundary, and we have tested several Lagrangian definitions in which the boundary is composed largely or entirely of invariant manifolds. These choices are influenced by the fact that potential vorticity can change considerably within a given lobe,

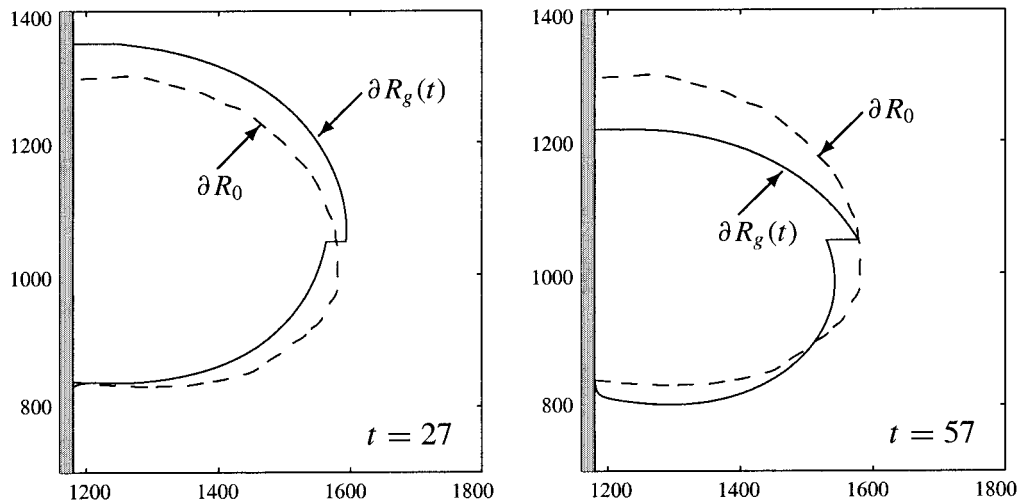


FIG. 14. Snapshots of the Lagrangian recirculation  $R_g(t)$  overlaid on the time-averaged recirculation  $R_0$ , for  $\delta_l = 95$  km. Note especially the variability in the location of the upper portion of the Lagrangian boundary, which results in significant mass transport across the fixed boundary  $\partial R_0$ .

making it difficult to explain the potential vorticity flux in terms of a simple turnstile mechanism. Of the two Lagrangian schemes tried, the one that uses sections of stable and unstable manifolds joined by a gate is the most straightforward. Since advection can occur only as a result of flow through the gate, the advective potential vorticity flux is easily calculated and visualized. A second approach is based on redefining the boundary in such a way that one lobe at a time is expelled or absorbed into the recirculation. The *apparent* potential vorticity flux calculated thereby agrees qualitatively with the result of the gate method. When the boundary is redefined to accommodate compensating pairs of lobes (the turnstile approach), the apparent potential vorticity flux differs substantially from the first two approaches due to the significant changes in potential vorticity over the longer redefinition time interval.

Regardless of the formulation, the wind stress curl (measured by the contour integral of the tangential wind stress around the boundary) is the main generating mechanism for (anticyclonic) vorticity in the gyre. According to the Eulerian budget, advection of anticyclonic vorticity into the gyre can also be a significant source at certain times, as evidenced by the strong peaks in the “advection” curves labeled  $Q'_A$  in Fig. 10. However, when a Lagrangian definition is used (Fig. 12) these peaks in  $Q'_A$  are much less pronounced and the overall contribution of advection is diminished. This discrepancy suggests that the peaks and troughs of  $Q'_A$  in Fig. 10 are due in part to the recirculation passing as a whole back and forth across a fixed boundary, an effect that one might wish to filter out.

This is not to say that Lagrangian definitions of the recirculation boundary are always preferable. As  $\delta_l/\delta_M$  increases and the eddy motions around the circulation become more complex, the lobes become more dis-

torted and the bookkeeping required to perform the flux calculations becomes cumbersome, as illustrated in Fig. 15. One may question the practical or intuitive value of calculating dynamical fluxes across a boundary, which might be extremely convoluted and variable in time. These difficulties motivate the third question raised, namely: how far can and should the method be pushed? Our subjective answer based on the experience of generating the invariant manifolds and doing the bookkeeping is that little will be gained in the present problem beyond the value  $\delta_l/\delta_M \approx 2.75$ . This upper limit is based on our experience in quantifying the lobe transport at  $\delta_l/\delta_M = 2.50$  as presented in this paper and preliminary results from an additional simulation at  $\delta_l/\delta_M = 2.75$ . The calculations to extract the lobe dynamics become considerably more difficult as  $\delta_l/\delta_M$  increases and the identification of a Lagrangian circulation becomes even more ambiguous.

The range of  $\delta_l/\delta_M$  values over which the method of lobe dynamics can be considered useful is indicated by the shaded window in Fig. 7 spanning the instability threshold  $\delta_l/\delta_M \approx 1.8$  and the above outer limit  $\delta_l/\delta_M \approx 2.75$ . The extent to which any part of the real ocean lies within this window is unknown. For one thing, sub-grid-scale eddies parameterized in our numerical model may intervene in the turnstile process in unknown ways. Or, perhaps the time dependence of persistent features such as the Alboran and Tsugaru gyres and the Great Whirl may simply be too complicated for lobe dynamics to be helpful.

*Acknowledgments.* This work was partially supported by the Office of Naval Research under Grants N00014-99-1-0258 (Pratt), N00014-99-1-0029 (Miller), N00014-92-J-1481 (Jones), and by National Science Foundation Grant OCE-9616949 (Pratt and Helfrich).

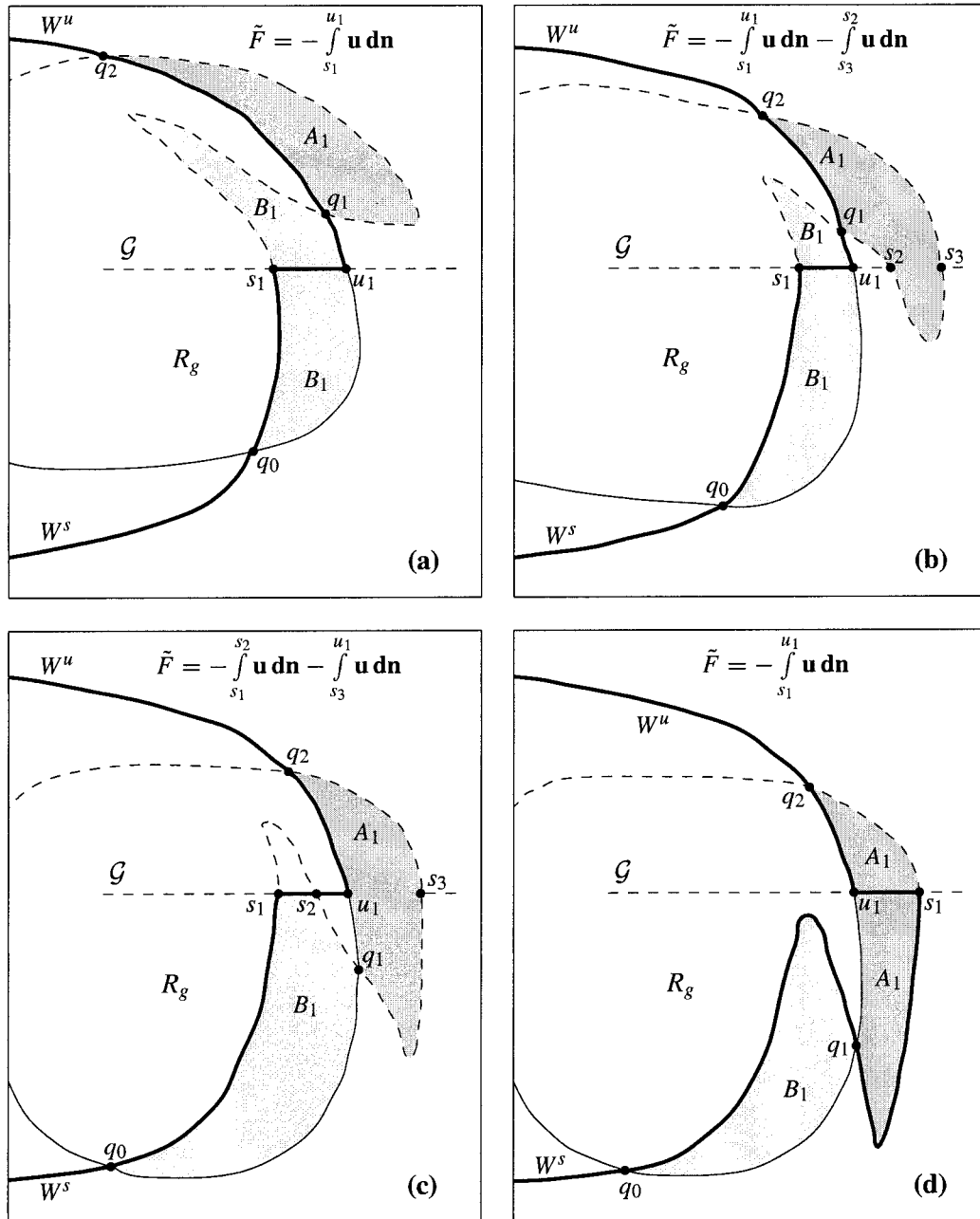


FIG. 15. Illustration of how transport across the gate  $\mathcal{G}[s_1, u_1]$  can differ from the description of transport via lobes. Frames (a)–(d) depict a situation where two lobes are crossing  $\mathcal{G}$  simultaneously. In (b) the segment  $\mathcal{G}[s_1, u_1]$  fails to capture the mass transport into the recirculation  $R_g$  associated with the second lobe  $A_1$ . In (c) transport across the gate segment  $\mathcal{G}[s_1, u_1]$  includes some transport that is not associated with lobe transport (the mass flux along the segment  $\mathcal{G}[s_2, u_1]$  is not associated with either of the lobes). At the same time there is still transport across  $\mathcal{G}[s_3, u_1]$ , which is not being accounted for. Frame (d) the manifolds shortly after the two intersections  $s_1$  and  $s_2$  have coalesced and disappeared, with  $s_3$  becoming the new  $s_1$ . At the point where  $s_1$  and  $s_2$  coalesce, the definition of the gate segment  $\mathcal{G}[s_1, u_1]$  is discontinuous as is the mass flux consistent with transport via lobes. The integrals for  $\tilde{F}$  in the upper right corner of each plot express the mass flux consistent with transport via lobes.

APPENDIX

Mass Fluxes Using a Gate

As described in section 4c, there are advantages to defining the boundary of the gyre as segments of stable and unstable manifolds joined by a nonmaterial surface, referred to as the gate. Referring to Fig. 15, the intersections of  $W_1^s$  with the reference line  $\mathcal{G}$  are labeled  $\{s_1, s_2, \dots\}$  where the ordering is with respect to increasing distance from the hyperbolic point  $p_1$  as measured along the curve  $W_1^s$  (see Fig. 15). Similarly, the intersections of  $W_2^u$  and  $\mathcal{G}$  are labeled  $\{u_1, u_2, \dots\}$  in terms of their distance from  $p_2$  along the curve  $W_2^u$ .

There are three main pieces making up the boundary of the recirculation  $R_g(t)$ : the first is the segment of  $W_1^s$  connecting  $p_1$  to  $s_1$ , the second is the gate  $\mathcal{G}[s_1, u_1]$ , and the third is the segment of  $W_2^u$  connecting  $u_2$  to the trajectory  $p_2$ . The island's boundary is used to close off the recirculation. For this definition of the recirculation  $R_g(t)$ , the (two-dimensional) mass flux at any time  $t$  is given by the integral  $F(t) = -\int_{s_1}^{u_1} \mathbf{u} \cdot \mathbf{n} ds$ . If the turnstile lobes are crossing the gate sequentially so that at any given time exactly one turnstile lobe intersects the gate, then there will be an exact correspondence between mass crossing the gate  $\mathcal{G}[s_1, u_1]$  and mass in the turnstile lobes. In this case the boundary of the gyre and the mass flux across  $\mathcal{G}[s_1, u_1]$  will vary continuously in time with the mass flux changing sign at  $t = t_0, t_1, \dots$ , and the mass in lobe  $k$  can be recovered exactly by integrating the expression for  $F(t)$  from  $t = t_{k-1}$  to  $t = t_k$ .

However, in the simulations presented here, it is possible for two turnstile lobes to intersect the gate at the same time, and the mass flux across  $\mathcal{G}[s_1, u_1]$  is not entirely consistent with the mass flux associated with the lobes. The way in which this usually occurs is illustrated in Fig. 15 where the meandering shape of the stable manifold  $W_1^s$  results in part of the incoming lobe  $A_1$  being ahead of a portion of the outgoing lobe  $B_1$  as they cross  $\mathcal{G}$ . Figure 15b shows the recirculation shortly after  $A_1$  has started to cross  $\mathcal{G}$ . In this case, accounting for all of the mass flux in the lobes requires a second line integral for the fluid transport in the trailing lobe  $A_1$ ,

$$\tilde{F} = -\int_{s_1}^{u_1} \mathbf{u} \cdot \mathbf{n} ds - \int_{s_3}^{s_2} \mathbf{u} \cdot \mathbf{n} ds.$$

Note that the second term in the flux calculation is integrated from  $s_3$  to  $s_2$  since this represents transport of fluid into the recirculation. In Fig. 15c the principal intersection  $q_1$  has crossed the gate  $\mathcal{G}$  and along with that, the intersection point  $s_2$  crosses over to the inside of the manifolds. Now the flux associated with the leading lobe  $B_1$  is just the integration from  $s_1$  to  $s_2$ , since fluid particles crossing  $\mathcal{G}[s_2, u_1]$  do not actually leave the recirculation as defined using turnstile lobes in section 3c. As in Fig. 15b, there is an additional flux term associated with lobe  $A_1$ ,

$$\tilde{F} = -\int_{s_1}^{s_2} \mathbf{u} \cdot \mathbf{n} ds - \int_{s_3}^{u_1} \mathbf{u} \cdot \mathbf{n} ds.$$

In passing from (c) to (d) in Fig. 15, the two intersection points  $s_1$  and  $s_2$  coalesce and disappear. At this point the location of  $s_1$  must jump to the intersection previously labeled  $s_3$ , resulting in a discontinuity in the boundary of the recirculation and initially some loss of symmetry as seen in part (d).

The situation illustrated in Fig. 15 can be partially eliminated by moving the gate  $\mathcal{G}$  farther around to the southern boundary of the recirculation. In this region the stable manifold is usually straight enough that the lobes are likely to be arranged with exactly one lobe crossing  $\mathcal{G}$  at any given time. However, the contribution to potential vorticity (pv) fluxes from the planetary vorticity is affected by the position of  $\mathcal{G}$  and, since one objective is to compare this analysis with the earlier results using the lobes, the flux calculations in section 4c are presented with  $\mathcal{G}$  placed at the midlatitude of the recirculation ( $y = 1050$  km). Moreover, computations show that there are not significant differences between the pv flux across  $\mathcal{G}[s_1, u_1]$  as characterized using (22) and the pv flux computed in the manner of  $\tilde{F}$  described in Fig. 15.

REFERENCES

- Beal, L. M., R. L. Molinari, T. K. Chereskin, and P. E. Robbins, 2000: Reversing bottom circulation in the Somali Basin. *Geophys. Res. Lett.*, **27**, 2565–2568.
- Bleck, R., C. Rooth, D. Hu, and L. T. Smith, 1992: Salinity-driven thermocline transients in a wind and thermohaline-forced isopycnal coordinate model of the North Atlantic. *J. Phys. Oceanogr.*, **22**, 1486–1505.
- Bowman, K. P., and P. J. Cohen, 1997: Exchange by seasonal modulation of the Hadley circulation. *J. Atmos. Sci.*, **54**, 2045–2059.
- Coulliette, C., and S. Wiggins, 2000: Intergyre transport in a wind-driven, quasigeostrophic double gyre: An application of lobe dynamics. *Nonlinear Proc. Geophys.*, **7**, 59–86.
- Duan, J., and S. Wiggins, 1996: Fluid exchange across a meandering jet with quasiperiodic variability. *J. Phys. Oceanogr.*, **26**, 1176–1188.
- , and —, 1997: Lagrangian transport and chaos in the near wake of the flow around an obstacle: A numerical implementation of lobe dynamics. *Nonlinear Proc. Geophys.*, **4**, 125–136.
- Godfrey, J. S., 1989: A Sverdrup model of the depth-integrated flow from the world ocean allowing for island circulations. *Geophys. Astrophys. Fluid Dyn.*, **45**, 89–112.
- Haller, G., and A. Poje, 1998: Finite-time transport in aperiodic flows. *Physica D*, **119**, 352–380.
- Holland, W. R., and P. B. Rhines, 1980: Example of eddy-induced ocean circulation. *J. Phys. Oceanogr.*, **10**, 1010–1031.
- Ierley, G. R., and W. R. Young, 1991: Viscous instabilities in the western boundary layer. *J. Phys. Oceanogr.*, **21**, 1323–1332.
- MacKay, R. S., J. D. Meiss, and I. C. Percival, 1984: Transport in Hamiltonian systems. *Physica D*, **13**, 55–81.
- Malhotra, N., and S. Wiggins, 1998: Geometric structures, lobe dynamics, and Lagrangian transport in flows with aperiodic time-dependence, with applications to Rossby wave flow. *J. Nonlinear Sci.*, **8**, 401–456.
- Miller, P., C. Jones, G. Haller, and L. Pratt, 1996: Chaotic mixing across oceanic jets. *Proc. AIP Conf. on Chaotic, Fractal, and*

- Nonlinear Signal Processing*, Mystic, CT, American Institute of Physics, 591–604.
- , —, A. M. Rogerson, and L. J. Pratt, 1997: Quantifying transport in numerically-generated velocity fields. *Physica D*, **110**, 105–122.
- Ngan, K., and T. G. Shepherd, 1997: Chaotic mixing and transport in Rossby-wave critical layers. *J. Fluid Mech.*, **334**, 315–351.
- Nof, D., and T. Pichevin, 1999: The establishment of the Tsugaru and the Alboran gyres. *J. Phys. Oceanogr.*, **29**, 39–54.
- Pedlosky, J., 1987: *Geophysical Fluid Dynamics*. Springer-Verlag, 710 pp.
- , 1996: *Ocean Circulation Theory*. Springer-Verlag, 480 pp.
- , L. J. Pratt, M. A. Spall, and K. R. Helfrich, 1997: Circulation around islands and ridges. *J. Mar. Res.*, **55**, 1199–1251.
- Poje, A., and G. Haller, 1999: Geometry of cross-stream mixing in a double-gyre ocean model. *J. Phys. Oceanogr.*, **29**, 1649–1665.
- Rogerson, A. M., P. D. Miller, L. J. Pratt, and C. K. R. T. Jones, 1999: Lagrangian motion and fluid exchange in a barotropic meandering jet. *J. Phys. Oceanogr.*, **29**, 2635–2655.
- Rom-Kedar, V., and S. Wiggins, 1990: Transport in two-dimensional maps. *J. Arch. Rat. Mech. Anal.*, **109**, 239–298.
- Samelson, R. M., 1992: Fluid exchange across a meandering jet. *J. Phys. Oceanogr.*, **22**, 431–440.
- Shariff, K., T. H. Pulliam, and J. M. Ottino, 1992: A dynamical systems analysis of kinematics in the time-periodic wake of a circular cylinder. *Vortex Dynamics and Vortex Methods*, C. Anderson and C. Greengard, Eds., *Lectures in Mathematics*, Amer. Math. Soc., 613–646.
- Vindez, A., J. M. Pinot, and R. L. Hanes, 1998: On the upper layer circulation in the Alboran Sea. *J. Geophys. Res.*, **103**, 653–666.
- Wiggins, S., 1992: *Chaotic Transport in Dynamical Systems*. Vol. 2, *Interdisciplinary Applied Mathematics*, Springer-Verlag, 301 pp.